J. Fluid Mech. (2025), *vol*. 1005, A10, doi:10.1017/jfm.2024.1222

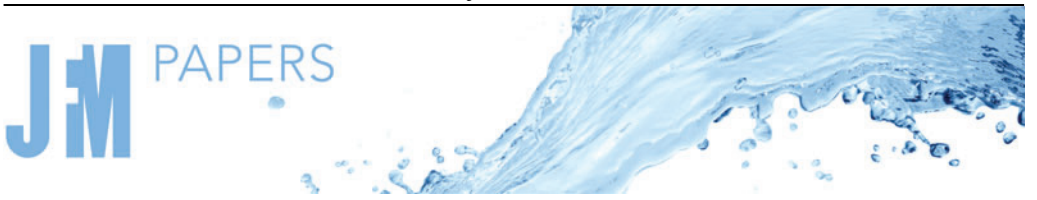

When does the elastic regime begin in viscoelastic pinch-off?

A. Gaillard[1],†, M.A. Herrada[2], A. Deblais[1], C. van Poelgeest[1], L. Laruelle[1], J. Eggers[3] and D. Bonn[2]

[1]Van der Waals-Zeeman Institute, University of Amsterdam, Science Park 904, 1098XH Amsterdam, The Netherlands

[2]Depto. de Mecánica de Fluidos e Ingeniería Aeroespacial, Universidad de Sevilla, Sevilla E-41092, Spain

[3]School of Mathematics, University of Bristol, University Walk, Bristol BS8 1TW, UK

(Received 6 June 2024; revised 30 October 2024; accepted 15 December 2024)

In this experimental and numerical study, we revisit the question of the onset of the elastic regime in viscoelastic pinch-off. This is relevant to all modern filament thinning techniques, which aim to measure the extensional properties of low-viscosity polymer solutions. Examples are the slow retraction method (SRM) for capillary breakup extensional rheometry (CaBER), or the dripping method, in which a drop detaches from a nozzle. As part of these techniques, a stable liquid bridge is brought slowly to its stability threshold, where capillary-driven thinning starts. This thinning slows down dramatically at a critical radius h_1, marking the onset of the elasto-capillary regime, characterised by a filament of nearly uniform radius. While a theoretical scaling exists for this transition in the case of the classical step-strain CaBER protocol, where polymer chains stretch without relaxing during the fast plate separation, we show that this theory is not necessarily valid for a slow protocol such as the SRM. In that case, polymer chains start stretching (beyond their equilibrium coiled configuration) only when the bridge thinning rate becomes comparable to the inverse of their relaxation time. We derive a universal scaling for h_1, valid for both low- and high-viscosity polymer solutions. This scaling is validated by CaBER experiments with a slow plate separation protocol using different polymer solutions, plate diameters and sample volumes, as well as by numerical simulations using the FENE-P model.

Key words: capillary flows, polymers

† Email address for correspondence: antoine0gaillard@gmail.com

1. Introduction

The elasticity of a polymer solution can be probed by stretching a drop between one's thumb and index finger, resulting in the formation of a filament with a persistence time that is linked to the relaxation time of the solution. Such filaments are observable in many industrial free-surface flows such as spraying (Keshavarz *et al.* 2015, 2016; Gaillard, Sijs & Bonn 2022) and inkjet printing (Christanti & Walker 2002; Sen *et al.* 2021), where long polymer molecules can be added to a Newtonian solvent to achieve a specific flow property, as well as in ejecta produced when coughing and sneezing (Scharfman *et al.* 2016; Gidreta & Kim 2023). The capillary-driven thinning dynamics of these filaments is the basis of numerous rheometry techniques dedicated to low-viscosity fluids, for which other techniques such as rheometric melt elongation (Meissner's RME) and filament stretching extensional rheometry (FiSER) are not applicable. These techniques include capillary breakup extensional rheometry (CaBER), where a droplet is confined between two plates that are separated beyond the range of stable liquid bridges (Bazilevsky *et al.* 1997; Stelter *et al.* 2000; Anna & McKinley 2001), the dripping technique where a droplet detaches from a nozzle (Amarouchene *et al.* 2001; Tirtaatmadja, McKinley & Cooper-White 2006; Rajesh, Thiévenaz & Sauret 2022), and dripping-onto-substrate (DoS), where a solid substrate is brought into contact with a drop hanging steadily from a nozzle (Dinic, Jimenez & Sharma 2017). All these techniques aim to creae a viscoelastic filament by triggering the pinching of a liquid column via the Rayleigh–Plateau instability.

Viscoelastic filaments are found to thin exponentially over time for a wide range of polymer-solvent systems and polymer concentrations (dilute and semi-dilute), consistent with the Oldroyd-B model, which predicts

$$h = h_1 \exp\left(-\frac{t - t_1}{3\tau}\right), \tag{1.1}$$

where h is the (minimum) filament radius, and τ is the relaxation time of the polymer solution, the longest one for a multimode model (Entov & Hinch 1997; Anna & McKinley 2001). This regime corresponds to an elasto-capillary balance where the elastic stress arising from the stretching of polymer chains balances the driving capillary pressure. Experimentally, starting from an equilibrium situation where polymers are relaxed (no pre-stress), this elastic regime can be observed only once polymers have been sufficiently stretched to overcome inertia and/or viscosity, which occurs at a time t_1 and at a filament radius $h_1 = h(t_1)$ marked by a sudden deceleration of the thinning dynamics.

The amount of stretching of polymer chains at times $t < t_1$ is set by the strength of the extensional flow in the pinching region. In the limit case where the thinning dynamics at times $t < t_1$ (before elasticity balances capillarity) is much faster than the solution's relaxation time – i.e. where polymer chains deform by the same amount as the surrounding solvent itself without relaxing – Clasen *et al.* (2006*a*) showed that the Oldroyd-B model leads to

$$h_1 = \left(\frac{G h_0^4}{2\gamma}\right)^{1/3}, \tag{1.2}$$

where γ is the surface tension, G is the elastic modulus and h_0 is the radius of the 'initial' liquid column before the onset of thinning, i.e. when the fluid is still at rest. This formula was first derived by Bazilevsky *et al.* (1997) and differs by a factor $2^{1/3}$ from the formula proposed by Entov & Hinch (1997), who did not treat the tension in the filament properly.

This 'relaxation-free' scenario leading to (1.2) corresponds to the step-strain CaBER protocol where the plates are separated so fast that polymer chains stretch without

having time to relax as the liquid bridge, connecting the two plates, stretches axially. In this step-strain protocol, the plates are separated exponentially over time to create an extensional flow with a constant extension rate $\dot{\epsilon}_0$ that, to ensure that polymer relaxation is negligible, must be larger that the coil–stretch transition value $1/2\tau$ (Miller, Clasen & Rothstein 2009). This corresponds to Weissenberg number $Wi_0 = \dot{\epsilon}_0\tau > 1/2$. Once the plates have reached their final separation distance L_F, the unstable liquid bridge between the two plates continues to thin, this time under the action of capillarity, until the elastic regime starts at a bridge/filament (minimum) radius h_1. Miller *et al.* (2009) showed that, consistent with (1.2), h_1 does not depend on L_F for polymer solutions. However, we could not find experimental studies where h_1 was reported and tested against (1.2) for different plate diameters and initial gaps, which set the radius h_0 of the initial (unloaded) fluid sample, or for different polymer solutions.

This step-strain CaBER protocol is, however, not recommended for low-viscosity polymer solutions since a fast plate separation leads to inertio-capillary oscillations of the end drops that hinder the measurement of the relaxation time (Rodd *et al.* 2005). Alternative protocols consist in reaching the threshold of the Rayleigh–Plateau instability slowly, e.g. by separating the plates at a constant low velocity in CaBER (slow retraction method or SRM) (Campo-Deano & Clasen 2010). In that case, the initially stable liquid bridge connecting the two end-plates becomes unstable at a critical plate separation distance, corresponding to a minimum bridge radius h_0, and thins further under the action of capillarity. This is similar to the dripping method where the bridge connecting a droplet to a nozzle, from which liquid is infused at a low flow rate, becomes unstable at a critical droplet weight (Rajesh *et al.* 2022).

In such slow protocols, (1.2) may not be valid if the time taken by the bridge to thin from its initial (minimum) radius h_0 to the radius h_1 (marking the onset of the elastic regime) is longer than the liquid's relaxation time τ, as was already noticed by Bazilevsky *et al.* (1997). In that case, polymer chains may indeed remain in a coiled state for a significant time, starting to stretch only when the bridge's thinning rate becomes comparable to $1/\tau$. This led Campo-Deano & Clasen (2010) to derive an alternative formula for h_1 for their slow retraction CaBER method that, to the best of our knowledge, has never been tested experimentally. In this formula, h_1 is independent of h_0, in sharp contrast with (1.2), which predicts $h_1 \propto h_0^{4/3}$. In a more recent experimental work from Rajesh *et al.* (2022), the authors proposed an empirical scaling $h_1 \propto R_n^{0.66}$ in dripping experiments with low-viscosity polymer solutions, where R_n is the nozzle radius, but they did not provide a theoretical explanation for their findings.

In such slow protocols, (1.2) is expected to be valid only if the time taken by the liquid bridge to thin from h_0 to h_1 is much shorter than the liquid's relaxation time, in which case polymer chains stretch without having time to relax. This time is expected to scale as the characteristic time scale of the capillary-driven bridge thinning dynamics derived from linear stability theory, namely, the Rayleigh (inertio-capillary) time scale (Wagner *et al.* 2005)

$$\tau_R = (\rho h_0^3/\gamma)^{1/2}, \tag{1.3}$$

or the visco-capillary time scale

$$\tau_{visc} = \eta_0 h_0/\gamma, \tag{1.4}$$

depending on the Ohnesorge number

$$Oh = \frac{\eta_0}{\sqrt{\rho\gamma h_0}} = \frac{\tau_{visc}}{\tau_R}, \tag{1.5}$$

where ρ and η_0 are the liquid density and total (zero-shear) viscosity, respectively. In other words, if we define a Deborah number

$$De = \tau/\tau_R \tag{1.6}$$

based on the Rayleigh time scale, then (1.2) is expected to be valid for $De \gg 1$ in the inviscid case ($Oh \ll 1$), and for $De/Oh = \tau/\tau_{visc} \gg 1$ in the viscous case ($Oh \gg 1$), which is the limit considered in most analytical studies (Clasen *et al.* 2006*a*).

In this study, we aim to expand our current understanding of the transition radius h_1 (marking the onset of the elastic regime) to cases where polymer relaxation is not negligible during the capillary-driven thinning of the liquid bridge. This discussion follows up on our previous paper, where h_1 was observed to increase linearly with h_0 for different liquids for a slow plate separation CaBER protocol (Gaillard *et al.* 2024), a scaling that differs from the $h_1 \propto h_0^{4/3}$ prediction of (1.2). Materials and methods are presented in § 2, and experimental results are presented in § 3. Theoretical expressions for h_1 are derived and tested experimentally and numerically using the Oldroyd-B model in § 4, and the FENE-P model in § 5.

2. Materials and methods

The liquids, their shear rheology and the experimental set-up and protocol are presented in §§ 2.1, 2.2 and 2.3, respectively. The equations and numerical methods are presented in § 2.4.

2.1. *Liquids*

Three of the polymer solutions used in the present study are the same as in our previous paper (Gaillard *et al.* 2024) and have comparable 'relaxation times' or, more precisely, comparable filament thinning rates. Two of them are solutions of poly(ethylene oxide) (PEO) of molecular weight $M_w = 4 \times 10^6\,\mathrm{g\,mol^{-1}}$ (PEO-4M), one in water with concentration 500 ppm, referred to as PEO_{aq}, and one in a ∼260 times more viscous solvent with concentration 25 ppm, referred to as PEO_{visc}. The third solution is a 1000 ppm solution of poly(acrylamide/sodium acrylate) (HPAM) [70 : 30] of molecular weight $M_w = 18 \times 10^6\,\mathrm{g\,mol^{-1}}$ in water with 1 wt% NaCl to screen electrostatic interactions and make polymer chains flexible instead of semi-rigid. Both polymers were provided by Polysciences (ref. 04030 for PEO and 18522 for HPAM). The solvent of the PEO_{visc} solution is a Newtonian 30 wt% aqueous solution of poly(ethylene glycol) (PEG) with molecular weight $20\,000\,\mathrm{g\,mol^{-1}}$ (PEG-20K). After slowly injecting the polymer powder into a vortex generated by a magnetic stirrer, solutions were homogenised using a mechanical stirrer at low rotation speed for approximately 16 h. For the PEO_{visc} solution, PEG was added after mixing PEO with water. Additional solutions of PEO-4M in water were prepared from dilution of a 10 000 ppm stock solution with concentrations ranging between 5 and 10 000 ppm to investigate the influence of polymer concentration.

2.2. *Shear rheology*

The shear viscosity η and first normal stress difference N_1 of polymer solutions were measured at the temperature of CaBER experiments, typically 20 °C, with an MRC-302 rheometer from Anton Paar equipped with a cone plate geometry (diameter 50 mm, angle 1°, and truncation gap 53 µm) and are shown in figure 1. To measure N_1, we follow

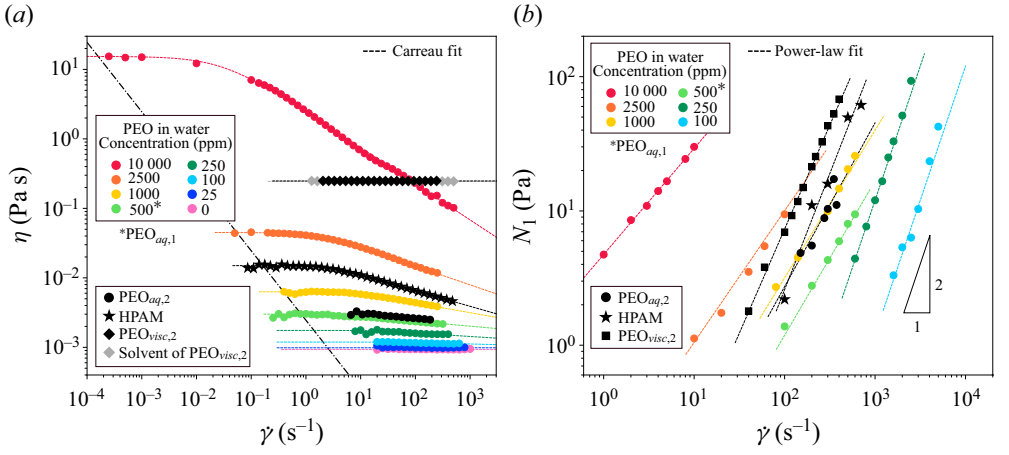

Figure 1. (*a*) Shear viscosity η and (*b*) first normal stress difference N_1 of the different polymer solutions against the shear rate $\dot{\gamma}$.

a step-by-step protocol similar to Casanellas *et al.* (2016) in order to circumvent the instrumental drift of the normal force. This protocol consists of applying steps of constant shear rate followed by steps of zero shear, and subtracting the two raw N_1 plateau values. The contribution of inertia to the normal force is corrected for by the rheometer (Macosko 1994). We find that the PEO$_{visc}$ solution is a Boger fluid with a constant shear viscosity, while the HPAM solution is shear-thinning, as well as the aqueous PEO solutions when concentrations are larger than 250 ppm. For shear-thinning solutions, the shear viscosity is fitted with the Carreau–Yasuda formula

$$\eta(\dot{\gamma}) = \eta_0 \left(1 + (\dot{\gamma}/\dot{\gamma}_c)^{a_1}\right)^{(n-1)/a_1}, \tag{2.1}$$

where η_0 is the zero-shear viscosity, n is the shear-thinning exponent, and $\dot{\gamma}_c$ is the shear rate marking the onset of shear thinning, with a_1 (typically 2) encoding the sharpness of the transition towards the shear-thinning regime. The polymer contribution to the shear viscosity $\eta_p = \eta_0 - \eta_s$ increases linearly with polymer concentration c in the dilute regime, and follows $\eta_p = \eta_s[\eta]c$, where, for the PEO solutions in water, we find an intrinsic viscosity $[\eta] = 2.87\,\mathrm{m^3\,kg^{-1}}$. Using the expression of Graessley (1980) gives a critical overlap concentration $c^* = 0.77/[\eta] = 0.268\,\mathrm{kg\,m^{-3}}$ (268 ppm), consistent with the onset of shear thinning expected at $c > c^*$. For the PEO$_{visc}$ solution, where only one concentration (25 ppm) was tested, assuming that the solution is dilute to calculate $[\eta]$ and c^* using the same formulas leads to a larger critical overlap concentration $c^* = 1400$ ppm, probably due to differences in polymer–solvent interactions (PEO in water versus PEO in PEG solution). The first normal stress difference is fitted by a power law

$$N_1 = \Psi_1 \dot{\gamma}^{\alpha_1}, \tag{2.2}$$

where we find $\alpha_1 = 2$ below c^*, and $\alpha_1 < 2$ above c^*, for aqueous PEO solutions, and $\alpha_1 < 2$ for the PEO$_{visc}$ and HPAM solutions. All fitting parameters are reported in table 1 for the PEO solutions of different concentrations in water, and in table 2 for the PEO$_{aq}$, PEO$_{visc}$ and HPAM solutions. We also report the density ρ and surface tension γ measured with a pendant drop method and, when known, the ratio c/c^*. Note that PEO addition reduces the surface tension of water since PEO is known to adsorb at the air/water interface (Gilányi *et al.* 2006). Surface tensions reported in tables 1 and 2 are the equilibrium ones.

c (ppm)	γ (mN m^{-1})	c/c^*	η_0 (mPa s)	η_p (mPa s)	n	$1/\dot{\gamma}_c$ (s)	α_1	Ψ_1 (Pa s$^{\alpha_1}$)
5	72.0	0.019	0.93	0.013	1	—	—	—
10	72.0	0.037	0.940	0.02	1	—	—	—
25	63.4	0.093	0.985	0.065	1	—	—	—
50	62.8	0.19	1.04	0.12	1	—	—	—
100	63.0	0.37	1.19	0.27	0.98	0.023	2	1.2×10^{-6}
250	63.0	0.93	1.75	0.83	0.95	0.054	2	1.2×10^{-5}
500	62.5	1.9	3.00	2.08	0.95	0.12	1.15	5.9×10^{-3}
1000	62.5	3.7	6.3	5.38	0.86	0.14	1.10	2.0×10^{-2}
2500	62.5	9.3	45	44	0.73	0.62	0.98	1.1×10^{-1}
10 000	62.3	37	15 400	15 400	0.48	34	0.79	4.7×10^{0}

Table 1. Concentration c, reduced concentration c/c^*, surface tension γ and shear rheological properties (from (2.1) and (2.2)) of aqueous PEO-4M solutions prepared from dilution of the same 10 000 ppm stock solution. Here, $\eta_p = \eta_0 - \eta_s$ is the polymer contribution to the shear viscosity. The density and solvent viscosity are $\rho = 998$ kg m^{-3} and $\eta_s = 0.92$ mPa s. The 500 ppm solution in this table is referred to as PEO$_{aq,1}$ in the text. For the 5 ppm solution, η_0 is too close to η_s to estimate η_p, and we therefore use $\eta_p = \eta_s[\eta]c$ with the intrinsic viscosity $[\eta]$ extracted from the linear fit of $\eta_p(c)$ for $c < c^*$.

Name	ρ (kg m^{-3})	γ (mN m^{-1})	η_s (mPa s)	c (ppm)	c/c^*	η_0 (mPa s)	η_p (mPa s)	n	$1/\dot{\gamma}_c$ (ms)	α_1	Ψ_1 (Pa s$^{\alpha_1}$)	τ_m (ms)
PEO$_{aq,2}$	998	62.5	0.92	500	1.9	3.3	2.08	0.93	120	1.2	9.9×10^{-3}	240
PEO$_{visc,2}$	1048	56.0	245	25	0.018	248	3.3	1	—	1.6	5.8×10^{-3}	110
HPAM	998	72.0	0.92	1000	—	15	14	0.78	410	1.7	9.0×10^{-3}	100

Table 2. Properties of the polymer solutions used for plate diameters $2R_0$ up to 25 mm in CaBER measurements. Here, ρ is the density, and γ is the surface tension. See the caption of table 1 for the definition of the shear properties. Also, τ_m is the maximum CaBER relaxation time measured for the largest plates; see figure 4(*a*). The PEO$_{visc,1}$ and PEO$_{visc,2}$ solutions have the same shear viscosity to within less than 5 %.

We must mention here that two different PEO$_{aq}$ solutions and two different PEO$_{visc}$ solutions have been used in this study, with differences in rheological properties in each case, caused by slightly different preparation protocols for a given recipe (e.g. a slightly different agitation time). The PEO$_{aq,1}$ solution is prepared from dilution of the same stock solution as the other aqueous PEO solutions in table 1. The PEO$_{aq,2}$ solution featured in table 2 exhibits a 10 % larger shear viscosity and approximately 2.5 times larger values of N_1, as shown in figure 1. The PEO$_{visc,1}$ and PEO$_{visc,2}$ solutions have the same shear viscosity to within less than 5 %, and only the latter one is presented in figure 1 and in table 2. As explained in § 2.3, the PEO$_{aq,1}$ and PEO$_{visc,1}$ solutions were tested with (CaBER) plate diameters less than 7 mm, varying the (non-dimensional) drop volume for each plate, whereas the PEO$_{aq,2}$ and PEO$_{visc,2}$ solutions were used for plate diameters up to 25 mm with a single (non-dimensional) drop volume for each plate.

2.3. *Experimental set-up and slow stepwise CaBER protocol*

The CaBER set-up and slow stepwise plate separation protocol described here are the same as in our previous paper (Gaillard *et al.* 2024). A droplet of volume V is placed on a horizontal plate of radius R_0, and the motor-controlled top plate of same radius is first moved down until it is fully wetted by the liquid, i.e. until the liquid bridge

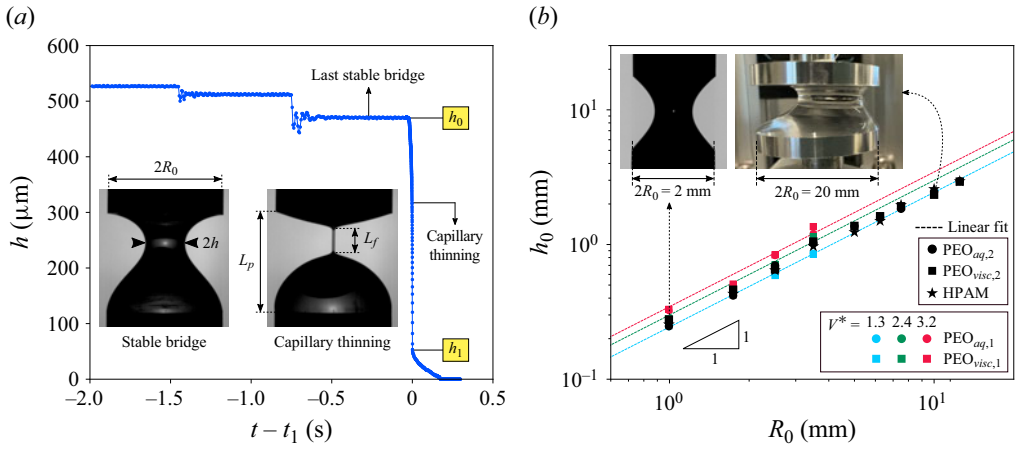

Figure 2. (*a*) Time evolution of the minimum bridge/filament radius h in our slow stepwise plate separation protocol for the PEO$_{aq,1}$ solution for plate diameter $2R_0 = 3.5$ mm and a sample volume $V^* = V/R_0^3 \approx 2.4$. Inset images correspond to a stable liquid bridge (left) and a thinning filament (right) of the same liquid, with $2R_0 = 7$ mm and $V^* \approx 2.4$. (*b*) Last stable bridge radius h_0 against the plate radius R_0: for $2R_0$ between 2 and 7 mm, and for each plate, $V^* \approx 1.3$, 2.4 and 3.2 for the PEO$_{aq,1}$ and PEO$_{visc,1}$ solutions; and for $2R_0$ between 2 and 25 mm, and a single volume ($V^* \approx 2.4$ for the smallest plates, and $V^* \approx 0.88$ for the largest plates) for the PEO$_{aq,2}$, PEO$_{visc,2}$ and HPAM solutions. Inset images correspond to stable liquid bridges ($h \geq h_0$) for $2R_0 = 2$ mm (left, PEO$_{aq,1}$ solution with $V^* \approx 2.4$) and $2R_0 = 20$ mm (right, HPAM solution with $V^* \approx 1.0$), the right-hand inset being taken from a phone camera because the lens of the set-up camera (used to take the other inset pictures) did not have a large enough field of view.

between the plates has a quasi-cylindrical shape. The top plate is then moved up slowly (at approximately 0.5 mm s^{-1}) and stopped at a plate separation distance L_p where the liquid bridge is still stable, as in the left-hand inset image of figure 2(*a*), but close to the bridge instability threshold. Then, instead of moving the top plate at a constant (lower) velocity, i.e. as in the SRM (Campo-Deano & Clasen 2010), we move it by 10 μm L_p-increment steps, waiting approximately one second between each step (longer than the solution's relaxation time), which is long enough to ensure that polymers are at equilibrium (no pre-stress) before each new step. At a certain step, the bridge becomes unstable (due to the Rayleigh–Plateau instability) and collapses under the action of surface tension, transiently leading to the formation of a nearly cylindrical filament that is the signature of viscoelastic pinch-off, as shown in the right-hand inset image of figure 2(*a*). We stop moving the top plate once we reach the step at which the bride collapses. The plate separation distance hence remains constant during the capillary thinning of the bridge/filament.

The process is recorded by a high-magnification objective mounted on a high-speed camera (Phantom TMX 7510), and images are analysed by a Python code. A typical time evolution of the minimum bridge/filament radius is shown in figure 2(*a*). Throughout the paper, we use the term 'bridge' for times $t < t_1$ before the onset of the elastic regime, and the term 'filament' during the elastic regime ($t \geq t_1$). This radius, measured at the thinnest point along the bridge/filament profile (see left-hand inset image in figure 2*a*) and labelled 'h_{min}' by many authors, is simply referred to as h in the rest of the paper. Note that each step can trigger small inertio-capillary oscillations that increase in intensity as the Rayleigh–Plateau instability threshold is approached; see figure 2(*a*), where oscillations vanish after approximately 0.2 s for the PEO$_{aq,1}$ solution. The purpose of this step-by-step plate separation protocol is to identify the last stable liquid bridge configuration and to

extract the value of its (minimum) radius h_0. Since steps are small, h_0 can be considered to be the initial bridge radius at the onset of capillary thinning. Our image resolution is up to 1 pixel per micrometre for the smallest drops, corresponding to the smallest plates, and our time resolution is 15 000 images per second to capture the fast bridge collapse from radius h_0 to the radius h_1 marking the onset of the elastic regime; see figure 2(*a*).

The liquid bridge becomes unstable at a critical plate separation distance $L_p = L_p^*$ marking the Rayleigh–Plateau instability threshold. The critical aspect ratio $\Lambda^* = L_p^*/(2R_0)$ depends on the liquid volume V and on the Bond number $Bo = \rho g R_0^2/\gamma$, where g is the gravitational acceleration (Slobozhanin & Perales 1993; Montanero & Ponce-Torres 2020). In our experiments, we vary the plate diameter $2R_0$ between 2 and 25 mm, as well as the non-dimensional sample volume

$$V^* = V/R_0^3. \tag{2.3}$$

Note that using R_0^3 as a reference volume is an arbitrary choice. Other authors often use the volume $\pi R_0^2 L_p^*$ between the plates. As shown in figure 2(*b*), the last stable bridge radius increases approximately linearly with the plate radius, i.e. $h_0 \propto R_0$ with a prefactor that increases with V^*, with no strong dependence on the liquid used since they all have comparable surface tensions. Typically, h_0/R_0 ranges between 0.24 and 0.35 for $V^* \approx 1.3$ and 3.2, respectively.

The size difference between the top and bottom end drops, visible in the inset images of figures 2(*a*,*b*), stems from Bond numbers $Bo = \rho g R_0^2/\gamma$ increasing from 0.16 to 25 as the plate size increases (Pingulkar, Peixinho & Crumeyrolle 2021). The 'filament' Bond number $Bo_f = \rho g L_f h_1/\gamma$, however, comparing the typical capillary pressure γ/h_1 in the filament to the hydrostatic pressure $\rho g L_f$ over the filament length L_f, is only up to 0.1 for the largest plate, indicating that the thinning dynamics is not driven by gravity. The filament length L_f, shown in the right-hand inset image of figure 2(*a*), is discussed in the Appendix.

The aluminium plates are plasma-treated before each measurement to increase their hydrophilicity and hence prevent dewetting of the top plate. However, dewetting could not be avoided for plate diameters $2R_0 \geq 10$ mm, as shown in the right-hand inset image of figure 2(*b*), featuring a stable liquid bridge ($h \geq h_0$) where the top end drop does not fully cover the top plate for $2R_0 = 20$ mm. Perhaps surprisingly, h_0 does not saturate at $2R_0 \geq 10$ mm in spite of this lack of full coverage; see figure 2(*b*). For such large plates, the top end drop is not necessarily at the centre of the top plate since the two plates are not perfectly parallel. Note that because of the plasma treatment, there is always a thin film covering the top plate.

All experiments are carried out at a high relative humidity (>80 %) ensured by placing the CaBER set-up in a box with wet paper tissues. We checked that repeating an experiment several times over the course of 10 min does not lead to any monotonic increase or decrease of the filament thinning rate (defined as $1/3\tau_e$; see § 3) over time, beyond small variations of less than 5 %, suggesting that both evaporation and polymer degradation (which may occur during bridge/filament thinning) are negligible.

2.4. *Equations and numerical methods*

The numerical simulations discussed in §§ 4 and 5 are performed using the FENE-P model, which aims to describe the stretching and finite extensibility of polymer chains. We consider a cylindrical axisymmetric (r, z) coordinate system aligned with the vertical axis

of the liquid bridge. In the simulations, we integrate the mass and momentum conservation equations of general form

$$\nabla \cdot \boldsymbol{v} = 0, \tag{2.4}$$

$$\rho \frac{\mathrm{D}\boldsymbol{v}}{\mathrm{D}t} = -\nabla p + \nabla \cdot \boldsymbol{\sigma}, \tag{2.5}$$

where ρ, $\boldsymbol{v} = v_r(r, z, t)\,\boldsymbol{e}_r + v_z(r, z, t)\,\boldsymbol{e}_z$ and $p(r, z, t)$ are the density, velocity and (reduced) pressure fields (accounting for gravity), respectively, and $\mathrm{D}/\mathrm{D}t$ is the material derivative. These equations are completed with the constitutive relationships for the stress tensor $\boldsymbol{\sigma} = \boldsymbol{\sigma}_s + \boldsymbol{\sigma}_p$, where

$$\boldsymbol{\sigma}_s = \eta_s \left(\nabla \boldsymbol{v} + (\nabla \boldsymbol{v})^{\mathrm{T}}\right) \tag{2.6}$$

is the contribution of the solvent of viscosity η_s, and $\boldsymbol{\sigma}_p$ is the polymer contribution. In the FENE-P model (Snoeijer *et al.* 2020), this contribution is calculated as

$$\boldsymbol{\sigma}_p = \frac{\eta_p}{\tau}\,(f\boldsymbol{A} - \boldsymbol{I}), \quad f = \frac{1}{1 - \mathrm{tr}(\boldsymbol{A})/L^2}, \tag{2.7a,b}$$

where η_p is the polymer contribution to the zero-shear viscosity $\eta_0 = \eta_s + \eta_p$, τ represents the relaxation time, and L^2 denotes the finite extensibility limit, with $\boldsymbol{I}$ the identity matrix. The conformation tensor $\boldsymbol{A}$ is calculated from the nonlinear relaxation law

$$\frac{\mathrm{D}\boldsymbol{A}}{\mathrm{D}t} - \left[(\nabla \boldsymbol{v})^{\mathrm{T}} \cdot \boldsymbol{A} + \boldsymbol{A} \cdot \nabla \boldsymbol{v}\right] = -\frac{1}{\tau}\,(f\boldsymbol{A} - \boldsymbol{I}). \tag{2.8}$$

The free-surface location is defined by the equation $r = h(z, t)$. The boundary conditions at that surface are

$$\frac{\partial h}{\partial t} + h_z w - u = 0, \tag{2.9}$$

$$-p + gz - \frac{hh_{zz} - 1 - h_z^2}{h(1 + h_z^2)^{3/2}} + \boldsymbol{n} \cdot \boldsymbol{\sigma} \cdot \boldsymbol{n} = 0, \tag{2.10}$$

$$\boldsymbol{t} \cdot \boldsymbol{\sigma} \cdot \boldsymbol{n} = 0, \tag{2.11}$$

where $h_z \equiv \partial h/\partial z$, $h_{zz} \equiv \partial^2 h/\partial z^2$, g is the gravitational acceleration, $\boldsymbol{n}$ is the unit outward normal vector, and $\boldsymbol{t}$ is the unit vector tangential to the free-surface meridians. Equation (2.9) is the kinematic compatibility condition, while (2.10) and (2.11) express the balance of normal and tangential stresses, respectively. The anchorage condition $h = R_0$ is set at $z = 0$ and $z = L_p$, where L_p is the plate separation distance. The no-slip boundary condition is imposed at the solid surfaces in contact with the liquid. The liquid volume V of the initial configuration is prescribed (and conserved), namely,

$$\pi \int_0^{L_p} h^2 \,\mathrm{d}z = V. \tag{2.12}$$

We start the simulation from a liquid bridge at equilibrium with a plate separation distance L_p just below (very close to) the critical one. The breakup process is triggered by applying a very small gravitational force perturbation. We refer to the minimum radius of the (stable) liquid bridge just before the perturbation is applied as h_0 due to the similarities with the experimental stepwise plate separation protocol described in § 2.3.

A numerical simulation is fully determined by five quantities: the Ohnesorge number, the Deborah number, the non-dimensional sample volume $V^* = V/R_0^3$, the finite extensibility parameter L^2, and the viscosity ratio

$$S = \eta_s/\eta_0. \tag{2.13}$$

While equations are non-dimensionalised using R_0 and $(\rho R_0^3/\gamma)^{1/2}$ as the characteristic length and time scales, in §§ 4 and 5 we refer only to values involving h_0 since, as we will show in § 3.1, it is h_0 (not R_0) that is the most relevant length scale of the problem. In particular, we refer to the Rayleigh and viscous time scales, and Ohnesorge and Deborah numbers defined in (1.3)–(1.6).

Simulations are performed in the absence of gravity where the threshold of the Rayleigh–Plateau instability – and therefore the shape of the initial bridge of minimum radius h_0 from which simulations start – is determined solely by V^*. In §§ 4 and 5, instead of referring to V^*, we refer to the value of h_0/R_0, since in experiments h_0/R_0 is set not only by V^* but also by the Bond number. We recall that in experiments, h_0/R_0 ranges between 0.24 and 0.35 for $V^* \approx 1.3$ and 3.2, respectively; see figure 2(*b*).

The model was solved with a variation of the method described in Herrada & Montanero (2016). The physical domain occupied by the liquid is mapped onto a rectangular domain through a coordinate transformation. Each variable, and its spatial and temporal derivatives appearing in the transformed equations, was written as a single symbolic vector. Then we used a symbolic toolbox to calculate the analytical Jacobians of all the equations with respect to the symbolic vector. Using these analytical Jacobians, we generated functions that could be evaluated in the iterations at each point of the discretised numerical domains.

The transformed spatial domain is discretised using $n_\eta = 11$ Chebyshev spectral collocation points in the transformed radial direction η of the domain. We used $n_\xi = 501$ equally spaced collocation points in the transformed axial direction ξ. The axial direction was discretised using second finite differences. Second-order backward finite differences were used to discretise the time domain. We used an automatic variable time step based on the norm of the difference between the solution calculated with a first-order approximation and that obtained from the second-order procedure. The nonlinear system of discretised equations was solved at each time step using the Newton method. The method is fully implicit.

3. Experimental results

In this experimental section, we investigate the roles of the plate radius and sample volume in § 3.1, and of the polymer concentration in § 3.2 on the pinch-off dynamics.

3.1. *Influence of the plate radius and sample volume*

Image sequences of the pinch-off dynamics are shown in figures 3(*a*) and 3(*b*) for the $\mathrm{PEO}_{aq,1}$ solution (500 ppm PEO-4M in water) and the $\mathrm{PEO}_{visc,1}$ solution (25 ppm PEO-4M in a $\sim$ 260 more viscous solvent), respectively, illustrating the transition from a bridge shape in the Newtonian regime to a filament shape in the elastic regime. For the $\mathrm{PEO}_{aq,1}$ solution, the filament is initially cylindrical until localised pinching is observed near one of the end drops (see frame 6 in figure 3*a*), followed by its destabilisation into a succession of beads connected by thin filaments (which are below our spatial resolution), a phenomenon usually referred to as 'blistering' instability (Sattler, Wagner & Eggers 2008; Sattler *et al.* 2012; Eggers 2014; Semakov *et al.* 2015) (see frames 7 and 8). For

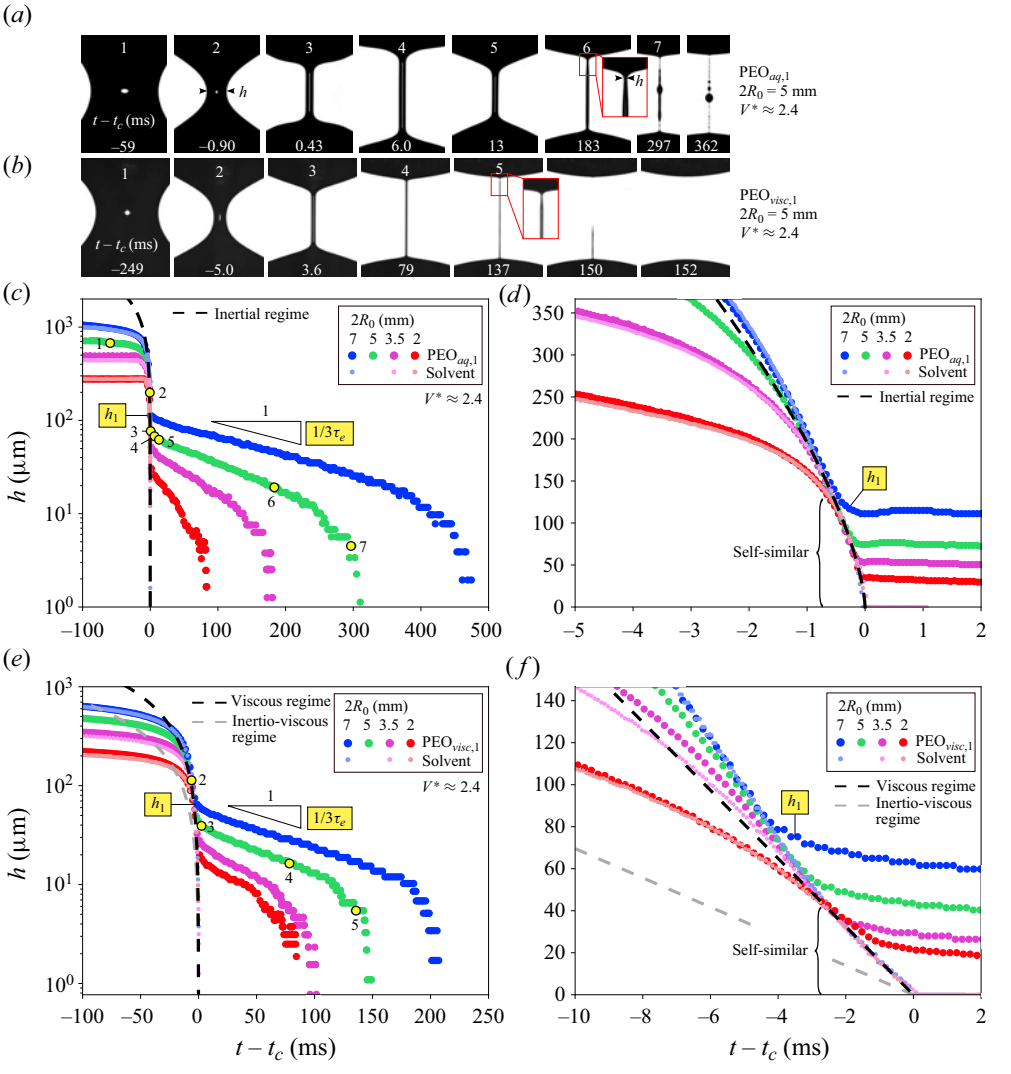

Figure 3. (*a*,*b*) Image sequences of the bridge/filament for the (*a*) PEO$_{aq,1}$ and (*b*) PEO$_{visc,1}$ solutions tested with plate diameter $2R_0 = 5$ mm and sample volume $V^* \approx 2.4$. (*c*–*f*) Time evolution of the minimum bridge/filament radius h in (*c*,*e*) semi-log and (*d*,*f*) lin–lin, for plate diameters $2R_0$ between 2 and 7 mm, and fixed $V^* \approx 2.4$, for the (*c*,*d*) PEO$_{aq,1}$ and (*e*,*f*) PEO$_{visc,1}$ solutions, and for their respective solvents (smaller data points), compared with (3.1) and (3.2), where t_c is the solvent breakup time. Times with labels 1–7 and 2–5 in (*c*,*e*), respectively, for $2R_0 = 5$ mm, correspond to the snapshots in (*a*,*b*).

the PEO$_{visc,1}$ solution, local pinching occurs very close to breakup, and no blistering is observed. In this paper, we refer to the minimum bridge/filament radius h, which therefore corresponds to the pinched region if localised pinching occurs. On another note, inertio-capillary oscillations of the top and bottom end drops lead to oscillations of the filament length for the PEO$_{aq,1}$ solution (see frames 3–6 in figure 3*a*). These oscillations are absent for the PEO$_{visc,1}$ solution due to viscous damping. Note that oscillations do not lead to significant oscillations of the filament radius, implying that when the length of the filament increases, new filament is being created from the liquid in the end drops.

Time evolutions of the minimum bridge/filament radius h are shown in figures 3(*c–f*) for four plate diameters between 2 and 7 mm, and a fixed non-dimensional sample volume $V^* \approx 2.4$ for the $\mathrm{PEO}_{aq,1}$ solution (figures 3*c*,*d*) and the $\mathrm{PEO}_{visc,1}$ solution (figures 3*e*,*f*) in semi-log (figures 3*c*,*e*) and lin–lin (figures 3*d*,*f*), the latter focusing on the transition to the elastic regime. The smaller data points correspond to the solvent alone for three of the same plate diameters, and in each case, the same V^* (to within experimental reproducibility). The time reference t_c corresponds to the critical time at which the bridge of solvent alone breaks up. For polymer solutions, since t_c cannot be determined, curves are shifted along the time axis until overlapping their corresponding solvent curves. The good overlap between polymer solutions and their solvent at all times $t < t_1$ (before the transition to the elastic regime) confirms that polymers do not affect the pinch-off dynamics in the (hence rightfully called) Newtonian regime. For the $\mathrm{PEO}_{visc,1}$ solution, where, as is about to be discussed, capillarity is balanced by viscosity in the Newtonian regime, this solution–solvent overlap is consistent with the low polymer contribution to the total shear viscosity ($\eta_p/\eta_0 = 0.013$). The least good solution–solvent overlaps are explained by experimental differences in V^*.

All curves corresponding to Newtonian solvents in figures 3(*d*,*f*) overlap close to breakup, indicating a self-similar thinning regime where the initial condition, set by R_0 and V^*, is forgotten. Such overlap is also observed for droplets of different volumes for a given plate radius. For the water solvent in figure 3(*d*), the self-similar regime is well captured by the inertio-capillary thinning law

$$h = A\left(\frac{\gamma}{\rho}\right)^{1/3}(t_c - t)^{2/3}, \tag{3.1}$$

with a prefactor $A = 0.47$ that is consistent with the experimental and numerical results of Deblais *et al.* (2018). For the ~ 260 times more viscous solvent in figure 3(*f*), the self-similar regime is well captured by the visco-capillary thinning law (Papageorgiou 1995; McKinley & Tripathi 2000)

$$h = 0.0709\,\frac{\gamma}{\eta_0}\,(t_c - t). \tag{3.2}$$

This is consistent with the fact that the Ohnesorge number $Oh = \eta_0/\sqrt{\rho\gamma h_0}$ (see (1.5)) is up to 0.02 for PEO_{aq}, and up to 0.1 for HPAM (for the smallest plate diameter where h_0 is lowest), i.e. $Oh \ll 1$, and ranges between 1.0 and 2.0 for the $\mathrm{PEO}_{visc,1}$ solution in the range of plate diameters considered in figure 3. In spite of the moderate Ohnesorge numbers in the latter case, we do not observe a clear transition to the inertio-visco-capillary thinning law $h = 0.0304(\gamma/\eta_0)(t_c - t)$ (Eggers 1993, 1997; Li & Sprittles 2016; Verbeke *et al.* 2020) that describes the behaviour of Newtonian fluids close to breakup; see figure 3(*d*).

Interestingly, the transition to the elastic regime occurs at approximately the time at which the self-similar Newtonian regime is reached in figures 3(*d*,*f*) – slightly after for the $\mathrm{PEO}_{aq,1}$ solution, and slightly before for the $\mathrm{PEO}_{visc,1}$ solution. However, in both cases, the transition radius $h_1 = h(t_1)$ increases with the plate diameter $2R_0$, which indicates that polymers already started to deform significantly before the self-similar regime. Indeed, if polymers started to deform only within the self-similar regime where the thinning dynamics no longer depends on R_0 or V^*, then the amount of polymer deformation would be independent of the initial condition, leading to a transition radius h_1 that would not depend on R_0 or V^*, as we discuss further in § 4.3.

After the filament formation, the thinning rate $|\dot{h}/h|$ is initially fairly constant, indicating an exponential decay, and increases close to breakup in a so-called 'terminal regime'

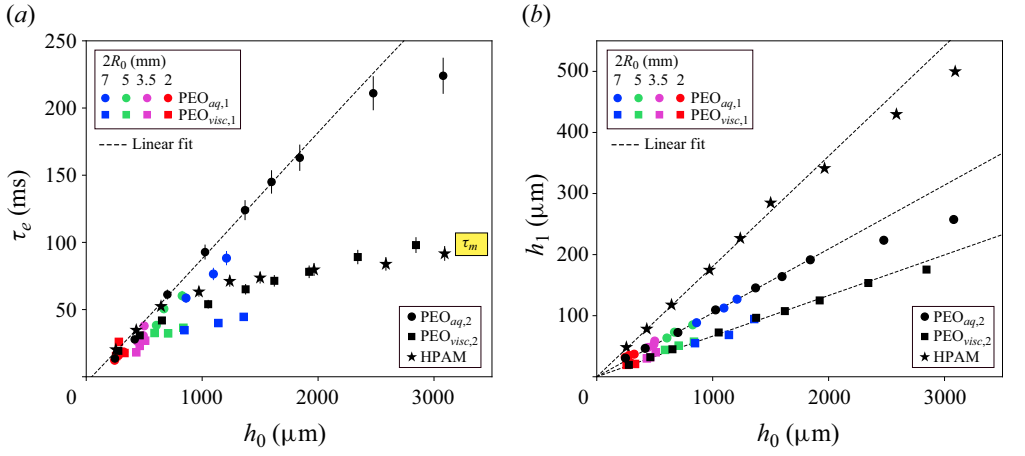

Figure 4. (*a*) Effective extensional relaxation time τ_e and (*b*) transition radius h_1 against the last stable bridge radius h_0 for different plate radii R_0 and sample volumes V^* for all polymer solutions. For the PEO$_{aq,1}$ and PEO$_{visc,1}$ solutions, three points of the same colour correspond to the same R_0 and three different $V^* \approx 1.3$, 2.4 and 3.2.

where authors argue that polymer chains approach full extension and a Newtonian-like high-viscosity dynamics is recovered (Anna & McKinley 2001; Stelter *et al.* 2002; Campo-Deano & Clasen 2010; Dinic & Sharma 2019). The (constant) filament thinning rate measured during the exponential part of the elastic regime is found to decrease with increasing plate diameter; see figures 3(*c*,*e*). This is inconsistent with the Oldroyd-B model, which predicts $|\dot{h}/h| = 1/3\tau$ (see (1.1)), where τ is the (longest) relaxation time of the polymer solution, which is a fluid property, independent of the size of the system. As we show in our previous paper (Gaillard *et al.* 2024), this surprising dependence on the system size is also observed for the classical step-strain plate separation protocol of a commercial CaBER rheometer as well as for DoS and dripping (Rajesh *et al.* 2022) experiments. We show that this is not caused by artefacts such as solvent evaporation or polymer degradation, suggesting that the liquid does not change when being tested with different plate diameters. To discuss this geometry-dependent filament thinning rate, we define an apparent (or effective) relaxation time τ_e such that $|\dot{h}/h| = 1/3\tau_e$ during the exponential part of the elastic regime.

The apparent relaxation time τ_e and the transition radius h_1 are plotted against h_0 in figure 4 for different polymer solutions, plate diameters $2R_0$ and non-dimensional sample volumes V^*. The fact that data corresponding to different values of R_0 and V^* collapse on a single curve for both the PEO$_{aq,1}$ and PEO$_{visc,1}$ solutions suggests that h_0, which is an increasing function of both R_0 and V^* (see figure 2*b*), is the only relevant geometrical parameter of the problem. This is the reason why we chose h_0 at the relevant length scale for non-dimensional numbers such as the Ohnesorge and Deborah numbers in (1.5) and (1.6). This is in agreement with the idea that the thinning dynamics is influenced only by extensional flow in the bridge/filament, while the top and bottom end droplets act as passive liquid reservoirs.

We find that τ_e seems to saturate towards a maximum value τ_m at large h_0; see figure 4(*a*). The estimated values of τ_m are reported in table 2 for the PEO$_{aq,2}$, PEO$_{visc,2}$ and HPAM solutions for which plate diameters up to 25 mm were used, well beyond typical CaBER plate sizes, which was needed to observe the saturation of τ_e. In our previous paper

(Gaillard *et al.* 2024), we explored the possibility that τ_m could be the 'real' relaxation time of the solution, invoking finite extensibility effects described by the FENE-P model to explain thinning rates larger than $1/3\tau_m$ for low h_0. We concluded that this was a possible explanation only for the $\mathrm{PEO}_{visc,2}$ solution, not for the $\mathrm{PEO}_{aq,2}$ and HPAM solutions, suggesting that the FENE-P model misses some important features of polymer dynamics in extensional flows.

The first transition radius h_1 increases approximately linearly with h_0 for all liquids; see figure 4(*b*). This is in contradiction with the scaling $h_1 \propto h_0^{4/3}$ expected from the Oldroyd-B model when assuming that polymer relaxation is negligible during the time needed for the bridge to thin from h_0 to h_1; see (1.2). Since $h_0 \propto R_0$ for a fixed V^* (see figure 2*b*), this implies that $h_1 \propto R_0$, different from the scaling $h_1 \propto R_n^{0.66}$ observed experimentally by Rajesh *et al.* (2022) in the analogous problem of a drop falling from a nozzle of radius R_n. This is surprising since R_n should play the same role as the plate radius R_0 in CaBER.

Note that the $\mathrm{PEO}_{aq,2}$ and $\mathrm{PEO}_{visc,2}$ solutions are slightly more elastic than the $\mathrm{PEO}_{aq,1}$ and $\mathrm{PEO}_{visc,1}$ solutions, since they exhibit larger apparent relaxation times; see figure 4(*a*). However, these differences are barely visible in figure 4(*b*) since the values of h_1 are almost the same, suggesting that the dependence of h_1 on τ_e is relatively weak, as we now confirm by varying the polymer concentration.

3.2. *Influence of the polymer concentration*

Figure 5 shows the time evolution of the minimum bridge/filament radius for the aqueous PEO solutions of table 1 of various PEO concentrations, water solvent included, that were tested for a fixed plate diameter $2R_0 = 3.5$ mm and sample volume $V^* \approx 2.4$, in semi-log (figure 5*a*) and in lin–lin focusing on the transition to the elastic regime (figure 5*b*). As in figure 3, the time t_c at which the solvent breaks is chosen as the time reference, and curves corresponding to polymer solutions are shifted along the time axis to maximise the overlap with the solvent for $t < t_1$. This overlap is very good up to 2500 ppm (dilute and unentangled semi-dilute solution), small deviations being attributable to slightly different sample volumes. For 10 000 ppm (entangled semi-dilute solution), however, the bridge dynamics prior to the exponential regime is radically different from the pure solvent case, indicating that elasticity is not negligible even before the exponential regime is reached.

The apparent relaxation time τ_e and the transition radius h_1 are plotted in figure 6 as functions of the polymer concentration c for the aqueous PEO solutions of table 1. Since these solutions were tested for a fixed plate diameter $2R_0 = 3.5$ mm and sample volume $V^* \approx 2.4$, the initial bridge radius $h_0 \approx 460\,\mu$m, also plotted in figure 6(*b*), is the same for each solution. For the 500 ppm solution, labelled $\mathrm{PEO}_{aq,1}$ – which was tested for four plate diameters from 2 to 7 mm, and in each case with three different volumes – the corresponding values of τ_e, h_0 and h_1 are also included in figure 6 to illustrate how data for a given concentration can shift as h_0 is varied. Although the plate diameters used for the $\mathrm{PEO}_{aq,1}$ solution were not large enough to estimate the high-h_0 limit value of τ_e, τ_m, the value estimated for the slightly more elastic $\mathrm{PEO}_{aq,2}$ solution (see figure 4(*a*) and table 2), is shown in figure 6(*a*) for $c = 500$ ppm.

We find a weak dependence $h_1 \propto c^{0.16}$ for dilute and semi-dilute solutions (see figure 6*b*), consistent with Rajesh *et al.* (2022), who found $h_1 \propto c^{0.15}$ in the analogous problem of a drop falling from a nozzle. We find a power law $\tau_e \propto c^{0.85}$ for the apparent relaxation time in figure 6(*a*), consistent with the wide range of exponents, typically between 0.6 and 1, reported by other authors in CaBER (Bazilevsky *et al.* 1997; Clasen

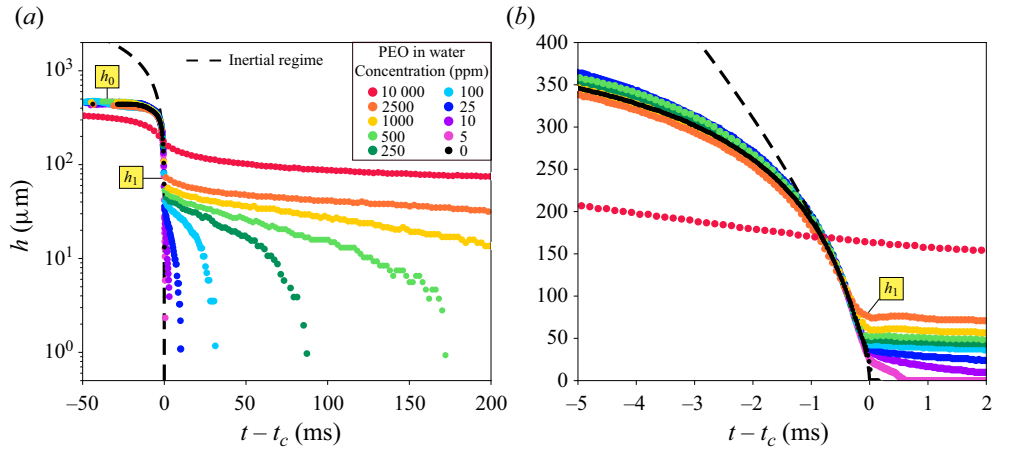

Figure 5. Time evolution of the minimum bridge/filament radius h in (*a*) lin–log and (*b*) lin–lin focusing on the transition, for PEO-4M solutions of different concentrations in water, for a fixed plate diameter $2R_0 = 3.5$ mm and sample volume $V^* \approx 2.4$. The time t_c is the time at which the bridge would break up for the solvent alone, here water.

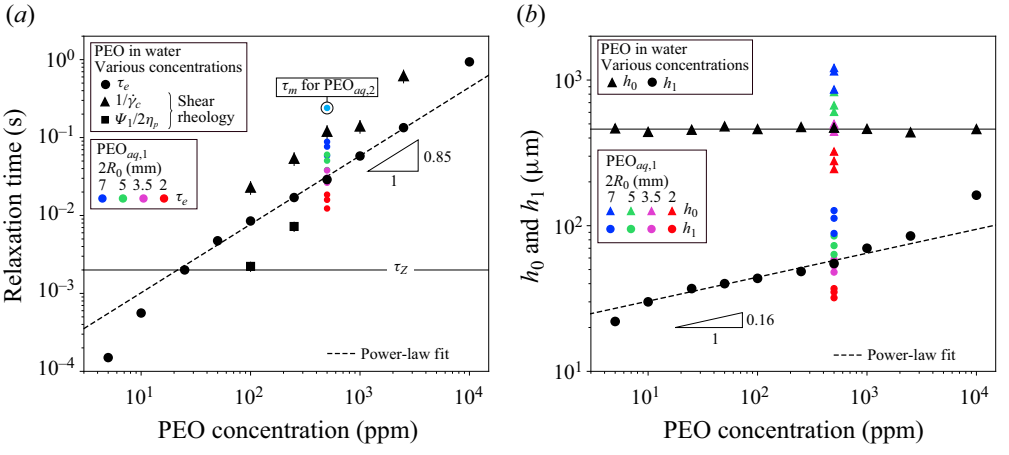

Figure 6. (*a*) Relaxation times and (*b*) transition radius h_1 and last stable bridge radius h_0 against polymer concentration for PEO-4M solutions of different concentrations in water. The data of (*b*) and the effective CaBER relaxation time τ_e in (*a*) correspond to a fixed plate diameter $2R_0 = 3.5$ mm and sample volume $V^* \approx 2.4$, except for the 500 ppm solution, where data corresponding to different $2R_0$ (between 2 and 7 mm) and V^* are shown. In (*a*), we also plot the relaxation time $1/\dot{\gamma}_c$ and $\Psi_1/2\eta_p$ inferred from shear rheology, as well as the Zimm relaxation time τ_Z. We also show the maximum CaBER relaxation time τ_m (high-h_0 limit of τ_e) measured for the (500 ppm) PEO$_{aq,2}$ solution (which is slightly more elastic than the PEO$_{aq,1}$ solution from which the other 500 ppm data points are taken; see figure 4*a*). Error bars are shown in (*a*) but are smaller than markers for τ_e.

et al. 2006*b*; Zell *et al.* 2010) and pendant drop experiments (Tirtaatmadja *et al.* 2006; Rajesh *et al.* 2022). Note that this exponent is expected to be a function of the solvent quality (Clasen *et al.* 2006*b*) and that its potential dependence on h_0 is not investigated in the present work. From these scalings, we deduce a weak dependence of $h_1 \propto \tau_e^{0.19}$ on the apparent relaxation time.

The apparent CaBER relaxation time τ_e in figure 6(*a*) is compared to values estimated from shear rheology, i.e. $1/\dot{\gamma}_c$, which is estimated from shear viscosity curves featuring shear thinning, which excludes low concentrations, and $\Psi_1/2\eta_p$, which is estimated from the first normal stress difference for the only two measurable solutions exhibiting a quadratic scaling $N_1 \propto \dot{\gamma}^2$. We observe that $1/\dot{\gamma}_c$ follows a power law with an exponent close to the one found for τ_e. Additionally, we find that τ_e is larger than $\Psi_1/2\eta_p$ in figure 6(*a*) for this specific plate radius, and would hence be even larger in the high-h_0 limit τ_m. Hence even for dilute solutions exhibiting weak shear thinning and quadratic normal stresses, for which the Oldroyd-B model could describe the shear rheology, there is no quantitative agreement between the relaxation time measured from normal stresses and that from filament thinning rheometry. This impossibility to quantitatively describe both shear and elongation properties with the Oldroyd-B model has also been reported by Zell *et al.* (2010), who dedicated a paper specifically to the link between τ_e and Ψ_1. In a recent perspective paper, Boyko & Stone (2024) suggest that the reason why elastic dumbbell models such as Oldroyd-B and FENE-P cannot quantitatively predict both shear and elongation properties of polymer solutions is because these models assume that, as in elongation flows, polymer chains approach full extension in strong shear flows ($\tau\dot{\gamma} \gg 1$), while experimentally, chains have been observed to extend only partially in strong shear flows due to their tumbling motion (Smith, Babcock & Chu 1999). The authors hence suggest that flows with both shear and elongational components should be described using more complex models such as the FENE-PTML model (Phan-Thien, Manero & Leal 1984), which captures this partial extension under shear. In this paper, we consider only filament thinning elongational flows for which Oldroyd-B and FENE-P are suitable model candidates.

As shown in figure 6(*a*), the apparent CaBER relaxation time τ_e increases in the dilute regime $c < c^*$. Moreover, for the most dilute solutions, τ_e is less than the Zimm relaxation time calculated using (Clasen *et al.* 2006*b*)

$$\tau_Z = \frac{1}{\zeta(3\nu)} \frac{[\eta] M_w \eta_s}{N_a k_B T}, \tag{3.3}$$

where N_a is the Avogadro number, k_B is the Boltzmann constant, T is the temperature, ζ is the Riemann zeta function, and ν is the solvent quality exponent. We used $\nu = 0.55$ between theta and good solvent to find $\tau_Z = 2.0\,\text{ms}$. Similar results were reported by Clasen *et al.* (2006*b*), who argue that the increase of τ_e in the dilute regime is caused by a self-concentration effect where chains start to interact while unravelling well beyond their equilibrium size in strong extensional flows. This was later rationalised by Prabhakar *et al.* (2016), who argue that the Zimm relaxation time is relevant only close to equilibrium, even for dilute solutions, and is not expected to accurately describe the relaxation behaviour of polymer chains in strong extensional flows such as in filament thinning. Clasen *et al.* (2006*b*) and Prabhakar *et al.* (2016), who considered only cases where inertia was negligible in the Newtonian regime, also show that values $\tau_e < \tau_Z$ arise at low polymer concentration where elasticity is too weak to fully overcome the solvent viscosity in the elastic regime. This effect should, however, be negligible for the aqueous PEO solutions of figure 6(*a*) since it is inertia (and not the solvent viscosity) that dominates in the Newtonian regime (see figure 5*b*). We show in § 5 that values $\tau_e < \tau_Z$ at low concentrations are consistent with polymer chains approaching their finite extensibility limit at the onset of the elastic regime (as anticipated by Campo-Deano & Clasen 2010), a case where (1.1) is no longer valid, and filament thinning rates $|\dot{h}/h| > 1/3\tau$ are to be expected, as we show in our previous paper (Gaillard *et al.* 2024).

4. Oldroyd-B prediction for h_1

In order to rationalise the experimental findings of § 3, we need to expand the polymer-relaxation-free theory leading to (1.2) for h_1 to cases where polymer relaxation is not negligible in the Newtonian regime. A generalised theoretical expression for h_1 based on the Oldroyd-B model is first derived in § 4.1. This expression is then tested against experimental results in § 4.2, before we use numerical simulations in § 4.3 to validate the theory and further explore the role of non-negligible polymer relaxation on h_1.

4.1. *Theory*

The filament radius $h_1 = h(t_1)$ marks the transition between the Newtonian regime ($t < t_1$), where the driving capillary force is balanced by inertia and/or viscosity, and the elastic regime ($t > t_1$), where capillarity is balanced by elastic stresses arising from the stretching of polymer chains. If inertia is negligible, then slender filament theory predicts that the total (unknown) tensile force T is constant along the liquid column (bridge or filament) (Eggers 1997; Clasen *et al.* 2006*a*), which, neglecting gravity and axial curvature effects, results in the zero-dimensional force balance equation (Clasen *et al.* 2006*b*)

$$(2X - 1)\,\frac{\gamma}{h} = 3\eta_s\dot{\epsilon} + \sigma_{p,zz} - \sigma_{p,rr}, \tag{4.1}$$

for a column of radius h. The driving capillary pressure γ/h is balanced by the normal stress difference $\sigma_{zz} - \sigma_{rr}$, which is the sum of the solvent viscous stress $3\eta_s\dot{\epsilon}$ and the polymeric stress $\sigma_{p,zz} - \sigma_{p,rr}$, where $\dot{\epsilon} = -2\dot{h}/h$ is the extension rate, the dot standing for $\mathrm{d}/\mathrm{d}t$, and z is the direction of the flow. The ratio $X = T/2\pi\gamma h$ may vary over time, approaching $X = 0.7127$ for a Newtonian fluid (McKinley & Tripathi 2000), hence recovering (3.2) close to breakup, and approaching $X = 3/2$ in the elastic regime for an Oldroyd-B fluid (Eggers, Herrada & Snoeijer 2020) (and not $X = 1$ as originally proposed in Entov & Hinch 1997). When inertia is not negligible, Tirtaatmadja *et al.* (2006) suggested adding a term of the form $\frac{1}{2}\rho\dot{h}^2$ to (4.1), from which the inertio-capillary scaling of (3.1) is recovered. In the elastic regime ($t > t_1$), assuming that inertia and/or solvent viscosity has become negligible, and assuming that the axial stress dominates the radial stress, i.e. $|\sigma_{p,rr}| \ll |\sigma_{p,zz}|$, the force balance equation reduces to

$$(2X - 1)\,\frac{\gamma}{h} = \sigma_{p,zz}. \tag{4.2}$$

The elastic regime starts when the polymeric axial stress $\sigma_{p,zz}$ – which increases over time in the Newtonian regime as polymer chains are progressively stretched by the extensional flow in the thinning bridge – becomes of the order of the capillary pressure, say, when it is equal to fraction p of the capillary pressure (Campo-Deano & Clasen (2010) chose $p = 1/2$). We hence get that $p\gamma/h_1 = \sigma_{p,zz}(t = t_1)$ where, for simplicity, the prefactor $2X - 1$ of order unity has been included in the prefactor p. To estimate h_1, we hence need to choose a constitutive equation to express the polymeric stress. Since our main goal is to understand the effect of polymer relaxation during the Newtonian regime on h_1, which, when negligible, leads to (1.2) for a single-mode Oldroyd-B fluid, we choose to use this model for simplicity. Indeed, although we know that the Oldroyd-B model is unable to capture the system-size dependence of the apparent relaxation time τ_e discussed in our previous paper (Gaillard *et al.* 2024) (see also figures 3 and 4*a*), it is not yet clear whether or not it is able capture h_1. Finite extensibility effects on h_1 will be discussed in § 5 using the FENE-P model.

For an Oldroyd-B fluid with elastic modulus G, we have $\sigma_{p,zz} = G(A_{zz} - 1)$, where A_{zz} is the normal part of the conformation tensor $\boldsymbol{A}$ that follows (see (2.8) and Wagner, Bourouiba & McKinley 2015)

$$\dot{A}_{zz} - 2\dot{\epsilon}A_{zz} = -\frac{A_{zz} - 1}{\tau}, \tag{4.3}$$

where τ is the relaxation time. Since we are interested in the location of highest polymer extensions along the bridge, we use the expression of the extension rate $\dot{\epsilon} = -2\dot{h}/h$ at the thinnest point to obtain

$$\dot{A}_{zz} + \frac{4\dot{h}}{h}A_{zz} = -\frac{A_{zz} - 1}{\tau}. \tag{4.4}$$

Some (as yet unknown) time after the onset of capillary thinning of the liquid bridge, polymer chains will have stretched well beyond their equilibrium size, i.e. $A_{zz} \gg 1$, so that the right-hand side of (4.4) reduces to $-A_{zz}/\tau$, at which point (4.4) can be integrated into

$$A_{zz}h^4 \propto \mathrm{e}^{-t/\tau}, \tag{4.5}$$

with an (as yet unknown) constant prefactor. Polymer chains are expected to remain close to their equilibrium coiled size (A_{zz} close to 1) until the extension rate in the thinning bridge approaches the coil–stretch transition value $1/2\tau$ predicted by the Oldroyd-B model. Beyond this point, following Clasen *et al.* (2009) and Campo-Deano & Clasen (2010), we assume that polymer chains unravel with negligible relaxation, i.e. that the right-hand side of (4.4) becomes negligible so that $A_{zz}h^4$ becomes constant. More precisely,

$$A_{zz}h^4 = H^4, \tag{4.6}$$

where H is the (as yet unknown) bridge radius at which relaxation becomes negligible, which should correspond to the coil–stretch transition point at which A_{zz} starts to become significantly larger than 1. In particular, at the transition to the elastic regime at time $t = t_1$,

$$A_1 = (H/h_1)^4, \tag{4.7}$$

where $A_1 = A_{zz}(t_1)$ quantifies the amount of polymer stretching at the onset of the elastic regime. Since $p\gamma/h_1 = \sigma_{p,zz}(t_1) = GA_1$, we finally get that

$$h_1 = \left(\frac{GH^4}{p\gamma}\right)^{1/3}, \tag{4.8}$$

which is different from (1.2). Indeed, while it is assumed that $H = h_0$ in the polymer-relaxation-free theory leading to (1.2), this is actually true only in the limit where polymer relaxation is negligible throughout the whole Newtonian regime so that $A_{zz}h^4$ is constant and equal to h_0^4 since $A_{zz} = 1$ at the onset of capillary thinning, assuming no pre-stress. In other words, in the limit where $H = h_0$, the coil–stretch transition starts at the onset of capillary thinning, which is expected to be true only if the relaxation time τ is much larger than the time taken by the liquid bridge to thin from h_0 to h_1. For completeness, in the elastic regime ($t \geq t_1$), combining (4.5) and (4.2) with $p\gamma/h_1 = GA_1$ leads to the exponential scalings $h = h_1 \exp(-(t - t_1)/3\tau)$ in (1.1) and $A_{zz} = A_1 \exp((t - t_1)/3\tau)$.

4.2. *Experiments*

We can now test the generalised expression (4.8) for h_1 against the experimental results of § 3. In order to do so, we first need to compute H from the time-evolution of A_{zz}. Note that we do not experimentally measure the extension of polymer chains, unlike Ingremeau & Kellay (2013), who confirmed the transition from a coiled to a stretched state in viscoelastic pinch-off using fluorescently labelled DNA. Rather, since our goal is to test a specific constitutive equation, here Oldroyd-B, we calculate its prediction for $A_{zz}(t)$ using (4.4), where the extension rate $\dot{\epsilon} = -2\dot{h}/h$ is taken from experimental values of $h(t)$. In other words, we calculate the prediction of the model for the experimental history of extension rates in the bridge/filament. In particular, we do not assume large polymer extension ($A_{zz} \gg 1$) since the point at which A_{zz} starts to become significantly larger than 1 is precisely what sets H. Equation (4.4) can in fact be integrated, as shown by Bazilevsky, Entov & Rozhkov (2001), introducing a function $y(t)$ such that $A_{zz} = y \exp(-t/\tau)/h^4$, which leads to $\dot{y} = h^4 \exp(t/\tau)/\tau$, yielding

$$A_{zz} = \frac{\mathrm{e}^{-t/\tau}}{h^4}\left(h_0^4\,\mathrm{e}^{t_0/\tau} + \frac{1}{\tau}\int_{t_0}^{t} h^4(t')\,\mathrm{e}^{t'/\tau}\,\mathrm{d}t'\right), \tag{4.9}$$

where the initial time t_0 corresponds to the onset of capillary thinning, i.e. $h(t_0) = h_0$ and $A_{zz}(t_0) = 1$ (no pre-stress). Since the $h(t)$ history is set by the experimental data, the only adjustable parameter of (4.9) is the relaxation time τ. In the following, we use either the apparent (τ_e) or the maximum (τ_m) relaxation time measured experimentally (see figure 4*a*) to calculate A_{zz} since we still do not know which is the 'true' one, if any.

Values of $A_{zz}(t)$ computed from (4.9) using the experimental values of $h(t)$ with relaxation time $\tau = \tau_m$ are shown in figure 7(*a*) for the PEO$_{aq,2}$ solution, and in figure 7(*b*) for the PEO$_{visc,2}$ solution, for plate diameters $2R_0$ between 2 and 20 mm. The experimental values of $h(t)$ are shown on the left-hand y-axis, and the time reference t_1 corresponds to the onset of the elastic regime. We find that the amount of polymer extension $A_1 = A_{zz}(t_1)$ at the onset of the elastic regime is fairly independent of the initial condition for the PEO$_{aq,2}$, while for the PEO$_{visc,2}$ solution, A_1 decreases as $h_0(R_0, V^*)$ increases, as mentioned in our previous paper (Gaillard *et al.* 2024), and as we are about to discuss here in more depth. In any case, we find that A_{zz} always increases as $1/h^4$ in the Newtonian regime close enough to the transition to the elastic regime. More specifically, values of A_{zz} are well captured by $(H/h)^4$ using H as a fitting parameter for each data set (close to t_1), from which H is estimated; see figure 7.

Values of H calculated using $\tau = \tau_m$, named $H(\tau_m)$, are plotted against h_0 in figure 8(*a*) for the PEO$_{aq,2}$, PEO$_{visc,2}$ and HPAM solutions, which are the only solutions for which sufficiently large plate diameters were used to estimate the maximum relaxation time τ_m (the high-h_0 limit of τ_e; see figure 4*a*). For the PEO$_{aq,2}$ and HPAM solutions, we find that H is essentially equal to h_0 at low h_0, and that H/h_0 decreases as h_0 increases, down to 0.73 for the largest plate diameter. In contrast, for the PEO$_{visc,2}$ solution, the ratio H/h_0 takes significantly smaller values, decreasing from 0.56 to 0.40 as h_0 increases. This is why the $(H/h)^4$ fit for A_{zz} is fairly good throughout the whole Newtonian regime for the PEO$_{aq,2}$ solution in figure 7(*a*), while it is valid only within a small time window close to the transition to the elastic regime for the PEO$_{visc,2}$ solution in figure 7(*b*). Indeed, if $H = h_0$, then the $(H/h)^4$ fit for A_{zz} is even valid at the onset of capillary thinning where $h = h_0$ and $A_{zz} = 1$.

Figure 8(*a*) hence suggests that although all three solutions have comparable relaxation times (see figure 4*a*), the thinning dynamics in the Newtonian regime is such that polymer

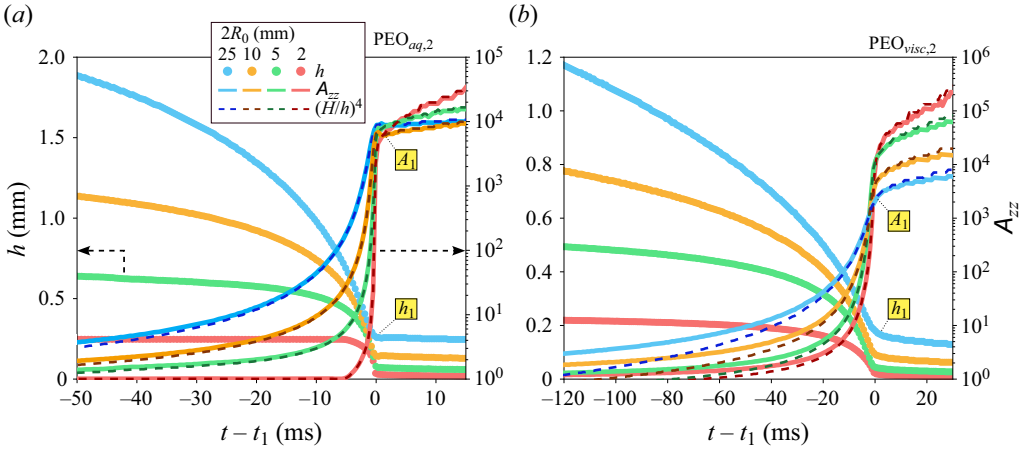

Figure 7. Time evolution of the experimental minimum bridge/filament radius h and of A_{zz}, calculated from the Oldroyd-B prediction (4.9) using the experimental values of $h(t)$ with the choice of relaxation time $\tau = \tau_m$ (see figure 4*a*), for plate diameters $2R_0 = 2$, 5, 10 and 25 mm for the (*a*) PEO$_{aq,2}$ and (*b*) PEO$_{visc,2}$ solutions. Time t_1 marks the onset of the elastic regime, with $h_1 = h(t_1)$ and $A_1 = A_{zz}(t_1)$. Values of A_{zz} in the Newtonian regime ($t < t_1$) are compared to $(H/h)^4$ (see (4.6)), where H is used as a fitting parameter to optimise the agreement close to t_1.

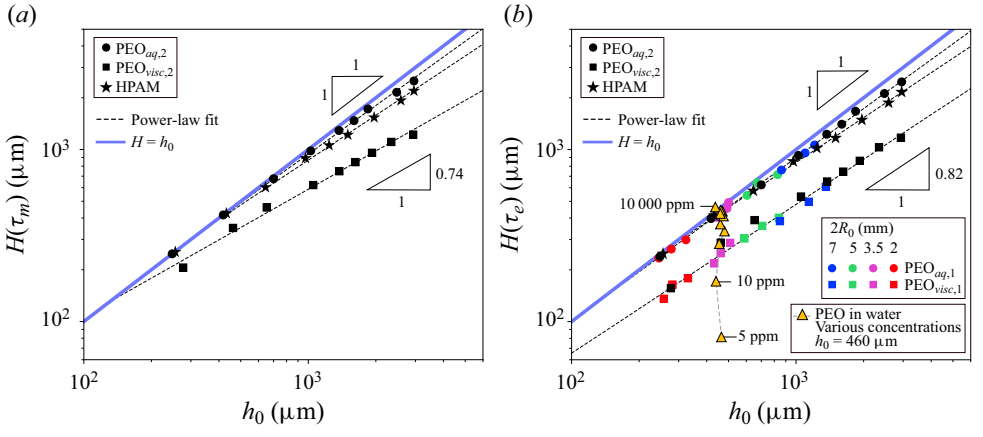

Figure 8. Values of H estimated from the time evolution of A_{zz} (calculated using Oldroyd-B; see figure 7) using (*a*) the maximum relaxation time $\tau = \tau_m$ or (*b*) the effective relaxation time $\tau = \tau_e$, for different polymer solutions and initial bridge radii $h_0(R_0, V^*)$, plotted against h_0. The line $H = h_0$ is shown in both plots.

chains stretch almost without relaxing in the Newtonian regime for the low solvent viscosity solutions (PEO$_{aq,2}$ and HPAM), while relaxation is not negligible for the high solvent viscosity (PEO$_{visc,2}$) solution. This is because the Newtonian thinning dynamics is slower for the most viscous solution; see e.g. figure 7, where, for $2R_0 = 2$ mm, the bridge takes only approximately 6 ms to thin from h_0 to h_1 for the PEO$_{aq,2}$ solution, much less than τ_m (chains do not have enough time to relax), while it takes approximately 900 ms for the PEO$_{visc,2}$, much more than τ_m (not visible in figure 7(*b*), where we focus on times close to t_1). The fact that H/h_0 increases as h_0 increases can therefore be interpreted by a longer time to thin from h_0 to h_1 as h_0 increases, consistent with the fact that the Rayleigh and viscous time scales $\tau_R = (\rho h_0^3/\gamma)^{1/2}$ and $\tau_{visc} = \eta_0 h_0/\gamma$ both increase with h_0.

The dependence of H on h_0 and on the solvent viscosity explains why, in figure 7 and in our previous paper (Gaillard *et al.* 2024), A_1 is independent of h_0 for low solvent viscosity solutions ($\mathrm{PEO}_{aq,2}$ and HPAM), while A_1 decreases as h_0 increases for the high solvent viscosity solution ($\mathrm{PEO}_{visc,2}$). For the former, where H is close to h_0 (negligible polymer relaxation in the Newtonian regime), $A_1 = (H/h_1)^4$ (see (4.7)) is close to $(h_0/h_1)^4$, which is fairly constant since $h_1 \propto h_0$ according to figure 4(*b*). For the latter, however, where $H \propto h_0^{0.74}$ in our range of h_0 according to figure 8(*a*), we get $A_1 = (H/h_1)^4 \propto h_0^{-1.04}$.

In figure 8(*b*), we plot the values of H, named $H(\tau_e)$, calculated using the apparent relaxation time $\tau = \tau_e$ when computing A_{zz} from (4.9) (instead of its large-h_0 limit τ_m in figure 8*a*). All polymer solutions are now featured since τ_e is measured for any experiment from an exponential fit of $h(t)$ in the exponential part of the elastic regime (see figure 3), i.e. the $\mathrm{PEO}_{aq,2}$, $\mathrm{PEO}_{visc,2}$ and HPAM solutions, as in figure 8(*a*), but also the $\mathrm{PEO}_{aq,1}$ and $\mathrm{PEO}_{visc,1}$ solutions, where three different non-dimensional sample volumes V^* were tested for each of the four smallest plate diameters, as well as the PEO solutions in water with various polymer concentrations (table 1), which were tested for a single (R_0, V^*) set corresponding to $h_0 \approx 460\,\mu\mathrm{m}$. The data corresponding to the PEO solutions with different polymer concentrations c show how, for a given flow history in the Newtonian regime (same $h(t)$ curves for $t < t_1$ for all concentrations; see figure 5), H increases with c via the increase in the relaxation time (here $\tau = \tau_e$), reaching the upper limit value h_0 at large τ. This is because for large τ values, polymer relaxation is negligible throughout the whole Newtonian regime, while for low τ values, A_{zz} remains equal to 1 for most of the Newtonian regime, increasing only when $\dot{\epsilon}$ is finally of the order of $1/2\tau$ close to the transition to the elastic regime.

Now that we know the value of H, we can test the validity of (4.8) for the filament radius h_1 at the onset of the elastic regime. The value of the elastic modulus, $G = \eta_p/\tau$ in the Oldroyd-B model, is, however, not uniquely defined, since while $\eta_p = \eta_0 - \eta_s$ can be calculated unambiguously from the shear rheology, the relaxation time τ could be either the apparent one τ_e or the maximum one τ_m, since we do not know yet which one is the 'true' one, if any. We hence need to test for both. To this end, we define

$$G_H = \gamma h_1^3/H^4, \tag{4.10}$$

where h_1 is the value measured experimentally, which should be $G_H = G/p$ according to (4.8).

In figure 9(*a*), G_H is plotted against G for the choice of relaxation time $\tau = \tau_m$ for the $\mathrm{PEO}_{aq,2}$, $\mathrm{PEO}_{visc,2}$ and HPAM solutions, which are the only solutions for which sufficiently large plate diameters were used to estimate τ_m. More precisely, values of $G_H(\tau_m)$ calculated from $H(\tau_m)$ are plotted against $G(\tau_m) = \eta_p/\tau_m$, which takes a unique value for each solution since the relaxation time is unique. We find that values of $G_H(\tau_m)$ are, however, not unique for the $\mathrm{PEO}_{aq,2}$ and HPAM solutions, and monotonically decrease as h_0 increases. For the $\mathrm{PEO}_{visc,2}$ solution, however, values of G_H vary between 0.11 and 0.23 without clear monotonic trend as h_0 increases. This is because, since $h_1 \propto h_0$ and $H \propto h_0^{k_H}$ in the range of h_0 values investigated, with $k_H \leq 1$ (see figures 4*b* and 8*a*), $G_H \propto h_1^3/H^4 \propto h_0^{3-4k_H}$, which means that G_H is expected to be independent of h_0 only for $k_H = 0.75$, very close to the value 0.74 found for the $\mathrm{PEO}_{visc,2}$ solution in figure 8(*a*). This suggests that the prediction of (4.8) for the choice $\tau = \tau_m$ is potentially valid for only one of our three solutions, the most dilute and viscous one.

By contrast, as shown in figure 9(*b*), when choosing τ_e instead of τ_m for the relaxation time to calculate $G_H(\tau_e)$ from $H(\tau_e)$ and $G(\tau_e) = \eta_p/\tau_e$, data points fall on a single curve

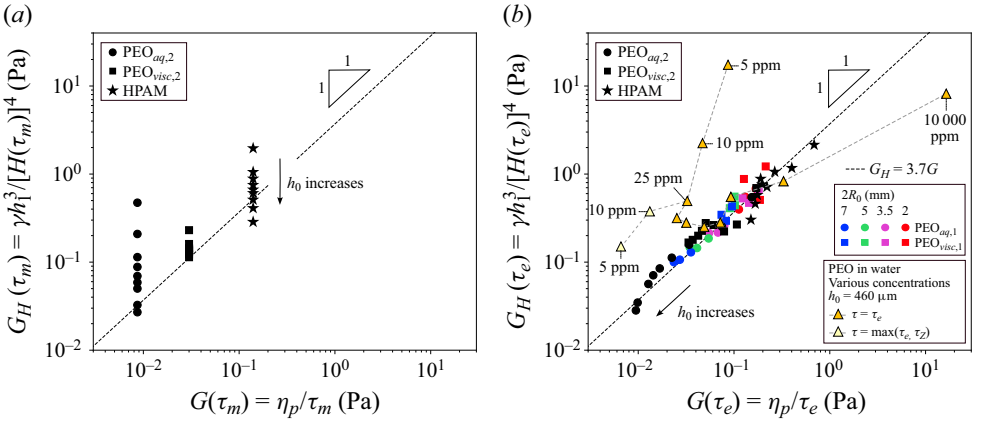

Figure 9. Values of G_H defined in (4.10) against the elastic modulus $G = \eta_p/\tau$, where H and G are calculated from (*a*) the maximum relaxation time $\tau = \tau_m$ or (*b*) the effective relaxation time $\tau = \tau_e$, for various polymer solutions and initial bridge radii $h_0(R_0, V^*)$. Values of h_1 are those measured experimentally. In (*b*), for the aqueous PEO solutions of different concentrations (see table 1), we show the effect replacing τ_e by the Zimm relaxation time τ_Z when calculating G and H for the lowest concentrations $c = 5$ and 10 ppm, which exhibit values of $\tau_e < \tau_Z$; see figure 6(*a*). The line $G_H = 3.7G$ is shown in both plots.

for all three solutions (PEO$_{aq,2}$, PEO$_{visc,2}$ and HPAM) as well as for the PEO$_{aq,1}$ and PEO$_{visc,1}$ solutions (for which V^* is varied for the four smallest plate diameters), and we find the linear relationship $G_H = G/p$ predicted by (4.8) with $p \approx 0.27$. It is quite remarkable that the Oldroyd-B model, derived for ideal dilute chains, is able to capture the transition to the elastic regime for solutions that are as diverse in terms of solvent viscosity, concentration and, potentially, solvent quality exponents.

Strong deviations from the $G_H = 3.7G$ line can be observed in figure 9(*b*) at low polymer concentrations for the data corresponding to the PEO solutions with various polymer concentrations. This data set can be broken down into three subsets: for typically $c < 100$ ppm, G_H decreases sharply with concentration, while is it almost constant for 100 ppm $\leq c < 2500$ ppm, and increases sharply with concentration for $c \geq 2500$ ppm. These trends can be explained by the fact that $G_H \propto h_1^3/H^4$, where h_1 increases very slowly with concentration as $h_1 \propto c^{0.16}$ for $c < 2500$ ppm, and increases sharply for higher concentrations (see figure 6*b*), while H increases sharply with concentration for typically $c < 100$ ppm, becoming almost constant and equal to h_0 for larger concentrations (see figure 8*b*). These strong deviations from the $G_H = 3.7G$ line observed at low polymer concentrations in figure 9(*b*) could be partially explained by the fact that apparent relaxation times (measured from exponential fitting of $h(t)$) are less than the Zimm relaxation time $\tau_Z = 2$ ms for $c = 5$ and 10 ppm (see figure 6*a*). In figure 9(*b*), we show the effect of choosing $\tau = \tau_Z$ instead of τ_e as the relaxation time for $c = 5$ and 10 ppm, which changes the value of both G_H via $H(\tau)$, and $G = \eta_p/\tau$. We find that this correction leads to data points significantly closer to the $G_H = 3.7G$ line, mainly stemming from values of H larger than in figure 8(*b*), although one order of magnitude deviation from the $G_H = 3.7G$ line remains. We show in § 5 that finite extensibility effects can explain this deviation (i.e. values of h_1 higher than the Oldroyd-B prediction) as well as the values of $\tau_e < \tau_Z$ for low polymer concentrations.

The large deviation from the $G_H = 3.7G$ line for the entangled 10 000 ppm solution in figure 9(*b*) (the only solution for which polymers affect the thinning dynamics even before

the exponential regime; see figure 5) is probably due to the fact that such solutions cannot be described by non-interacting polymer theories such as Oldroyd-B.

In conclusion, when polymer relaxation is not negligible in the Newtonian regime ($t < t_1$), (1.2) should be replaced by (4.8), which gives $h_1 \propto H^{4/3}$ where $H \leq h_0$. In our experiments, the power-law dependence of H on h_0 (see figure 8) leads to the fairly proportional relationship between h_1 and h_0 observed in figure 4(*b*), differences in slopes among different liquids stemming from differences in elastic moduli G. Now that we have established that it is H (and not h_0) that sets the transition to the elastic regime, we discuss in § 4.3 how it scales with the parameters of the problem, using numerical simulations to cover a wide range of parameters.

4.3. *Simulations*

To further investigate the effect of polymer relaxation on the transition radius h_1 marking the onset of the elastic regime, we now consider numerical simulations using the Oldroyd-B model ($L^2 = +\infty$) with a single relaxation time τ (finite extensibility effects will be discussed in § 5). In this paper, numerical simulations are not directly compared to experiments but are rather used to validate theoretical expressions that are then compared with experiments (see our previous paper for direct experiment–simulation comparisons; Gaillard *et al.* 2024).

In order to capture h_1, we first need to capture the critical bridge radius H at which polymer relaxation (the right-hand side of (4.3) or (2.8)) becomes negligible in the Newtonian regime ($t < t_1$). The bridge radius H marks the onset of the coil–stretch transition at which polymer chains start to extend significantly beyond their equilibrium shape, i.e. at which A_{zz} starts becoming significantly larger than 1; see § 4.1. We already know that $H \to h_0$ in the limit where the relaxation time τ is so large that polymer relaxation is always negligible in the Newtonian regime, a limit where (4.8) reduces to the classical formula (1.2). The goal of this subsection is therefore to expand our knowledge to cases where relaxation is not negligible in the Newtonian regime using the Oldroyd-B model.

Figure 10 shows the numerical time evolution of the non-dimensional minimum bridge/filament radius h/h_0 for a fixed Ohnesorge number $Oh = 2.07$, viscosity ratio $S = 0.988$ and $h_0/R_0 = 0.23$, with three Deborah numbers De spanning four orders of magnitude (see (1.5), (1.6) and (2.13) for definitions). We consider only the value of A_{zz} at this minimum-radius position along the bridge/filament since this is where polymer chains are the most stretched. This maximum value, simply denoted A_{zz} from now on, is plotted in figure 10 on the right-hand y-axis. Note that all h/h_0 curves are identical in the Newtonian regime, diverging only at the transition to the elastic regime at different radii h_1. The time reference t_c corresponds to the time at which the bridge would break if this transition did not occur. This is highlighted by the fact that the self-similar viscous thinning law (3.2), which becomes $h/h_0 = 0.0709(t_c - t)/(Oh\,\tau_R)$ with our choice of non-dimensionalisation, and which is plotted in figure 10, fits numerical results close to the transition. Note that simulations could often not be continued long after the transition.

Figure 10 shows how, for a given flow history in the Newtonian regime, polymer chains start stretching at different times depending on the Deborah number. For $De \gg 1$, relaxation is always negligible in the Newtonian regime, and A_{zz} therefore increases as $(H/h)^4$ where $H = h_0$; see the discussion in § 4.1. For $De \ll 1$, however, the flow becomes strong enough to start stretching polymers (beyond their equilibrium shape) only at small bridge radii where the thinning dynamics has become self-similar and, for $Oh \gg 1$, follows

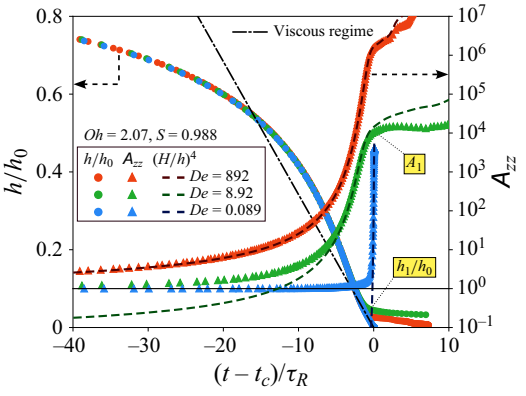

Figure 10. Numerical time evolution of the non-dimensional (minimum) bridge/filament radius h/h_0 and of the (maximum) polymer extension A_{zz} for $Oh = 2.07$, $S = 0.988$ and $h_0/R_0 = 0.23$, and three different Deborah numbers. Values of A_{zz} are compared with $(H/h)^4$ close to the onset of the elastic regime, where H is used as a fitting parameter. The self-similar viscous regime of (3.2), or equivalently $h/h_0 = 0.0709(t_c - t)/(Oh\,\tau_R)$, is also plotted, where t_c is the time at which the filament would break if the transition to an elastic regime, at $h = h_1$, did not occur.

(3.2). In that case, $A_{zz} = 1$ for most of the Newtonian regime, increasing only close to the transition to the elastic regime, following $A_{zz} = (H/h)^4$ where $H \ll h_0$ is the characteristic bridge radius at which A_{zz} starts increasing. Values of H are estimated by fitting A_{zz} with $(H/h)^4$, using H as a fitting parameter (see figure 10), as was done in figure 7 for experimental results.

Values of H/h_0 are plotted against the Deborah number in figure 11(a) for Ohnesorge numbers between 0.2 and 20. The low-De behaviour corresponds to cases where polymers start stretching only within the self-similar regime where the thinning dynamics follows a scaling of the form $h = B(t_c - t)^\beta$, with $B \sim (\gamma/\rho)^{1/3}$ and $\beta = 2/3$ in the inviscid limit ($Oh \ll 1$; see (3.1)), and $B \sim \gamma/\eta_0$ and $\beta = 1$ in the viscous limit ($Oh \gg 1$; see (3.2)). The coil–stretch transition occurs when the extension rate $\dot{\epsilon} = -2\dot{h}/h = 2\beta/(t_c - t)$ becomes of the order of $1/\tau$, i.e. at a time $t_H = t_c - 2\beta\tau$. Therefore, the bridge radius $H = h(t_H)$ marking the onset of the coil–stretch transition scales as

$$H \sim (\gamma\tau^2/\rho)^{1/3} \quad \Leftrightarrow \quad H/h_0 \sim De^{2/3} \tag{4.11}$$

in the inviscid limit ($Oh \ll 1$), as first derived by Campo-Deano & Clasen (2010), or as

$$H \sim \gamma\tau/\eta_0 \quad \Leftrightarrow \quad H/h_0 \sim De/Oh = \tau/\tau_{visc} \tag{4.12}$$

in the viscous limit ($Oh \gg 1$). The scaling of (4.12) is shown in figure 11(a) with a prefactor 0.2, and shows good agreement with the values of H for the two largest Ohnesorge numbers. Unfortunately, no simulations could be performed for $Oh \ll 1$ to test (4.11). Note that in this peculiar limit where polymer chains start stretching only within the self-similar thinning regime, H – and therefore h_1 given by (4.8) – does not depend on h_0 and is therefore independent of the size of the system, in sharp contrast with the high-De limit, where $H = h_0$ and therefore $h_1 \propto h_0^{4/3}$; see (1.2). In fact, inserting (4.11) or (4.12) into (4.8) gives

$$h_1 \sim (G(\gamma\tau^8/\rho^4)^{1/3})^{1/3} \tag{4.13}$$

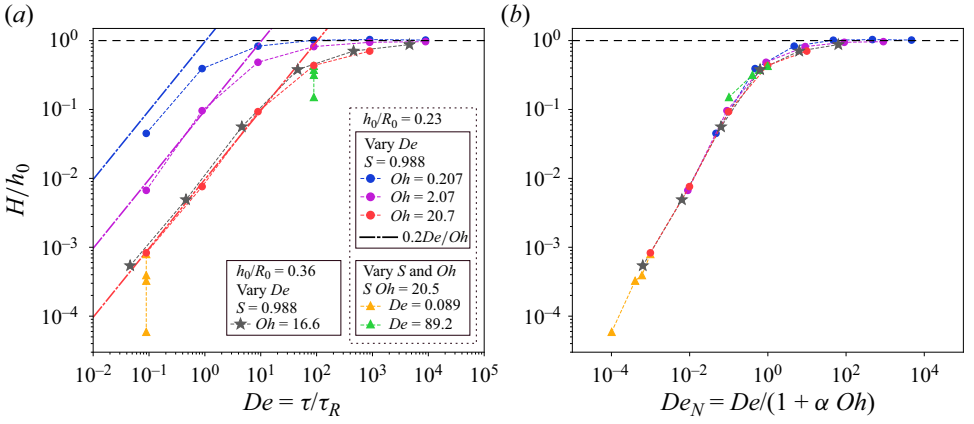

Figure 11. Numerical values of H/h_0 against (a) the Deborah number $De = \tau/\tau_R$ based on the inertio-capillary time scale τ_R, and (b) the general Deborah number $De_N = \tau/\tau_N$ based on the general time scale $\tau_N = \tau_R(1 + \alpha Oh)$ with $\alpha = 4.3$, for various parameters (the same in (a) and (b)). Dots (•) correspond to $h_0/R_0 = 0.23$ and $S = 0.988$, with $Oh = 0.207$ (blue) $Oh = 2.07$ (purple) and $Oh = 20.7$ (red), and De ranging between 8.92×10^{-2} and 8.92×10^3 (last De excluded for the largest Oh). Triangles (▲) correspond to $h_0/R_0 = 0.23$ with $De = 8.92 \times 10^{-2}$ (yellow) and $De = 8.92 \times 10^1$ (green), varying both S (between 0.1 and 0.988) and Oh while keeping $S\,Oh$ constant and equal to 9.88. Stars (⋆) correspond to $h_0/R_0 = 0.362$ with $Oh = 16.6$ and $S = 0.988$, and De ranging between 4.59×10^{-2} and 8.92×10^3.

in the inviscid limit ($Oh \ll 1$), or

$$h_1 \sim (G\gamma^3\tau^4/\eta_0^4)^{1/3} \tag{4.14}$$

in the viscous limit ($Oh \gg 1$).

In the high-De limit, $H/h_0 \to 1$ since polymer relaxation becomes negligible even at the onset of capillary thinning where $h = h_0$. However, while all curves in figure 11(a) have the same shape, the Deborah number at which H/h_0 reaches 1 depends on the Ohnesorge number. This is because we chose to express the Deborah number as $De = \tau/\tau_R$, where $\tau_R = (\rho h_0^3/\gamma)^{1/2}$ is the inertio-capillary time scale, which is not relevant for the moderate to large Ohnesorge number featured in figure 11(a). The relevant time scale for the thinning dynamics at large Oh is $\tau_{visc} = Oh\,\tau_R = \eta_0 h_0/\gamma$, and we would hence expect that $H/h_0 = O(1)$ not when $\tau/\tau_R = O(1)$ but when $\tau/\tau_{visc}(= De/Oh) = O(1)$. In figure 11($b$), we show that values of H/h_0 indeed rescale on a single curve when plotted against a generalised Deborah number $De_N = \tau/\tau_N$, where τ_N, defined as

$$\tau_N = \tau_R(1 + \alpha\, Oh), \tag{4.15}$$

is an empirical attempt at expressing the general time scale of the thinning dynamics in the Newtonian regime for any Oh, connecting the low- and high-Oh scalings τ_R and τ_{visc}, where $\alpha = 4.3$ is a fitting parameter. This scaling ensures that $H/h_0 = O(1)$ when $De_N = O(1)$ for any Ohnesorge number. However, according to (4.11) and (4.12), we expect different scalings for $De_N \ll 1$, namely, $H/h_0 \sim De_N^{2/3}$ for $Oh \ll 1$ and $H/h_0 \sim De_N$ for $Oh \gg 1$.

So far, we have varied De and Oh for a fixed viscosity ratio $S = 0.988$ and a fixed sample volume characterised by a fixed value of $h_0/R_0 = 0.23$. In order to further investigate the generality of the H/h_0 dependence on De_N identified in figure 11(b), we therefore performed additional simulations. Two sets of simulations were performed for $De = 0.089$ and 89.2, respectively, keeping $h_0/R_0 = 0.23$, where both S and Oh were varied while

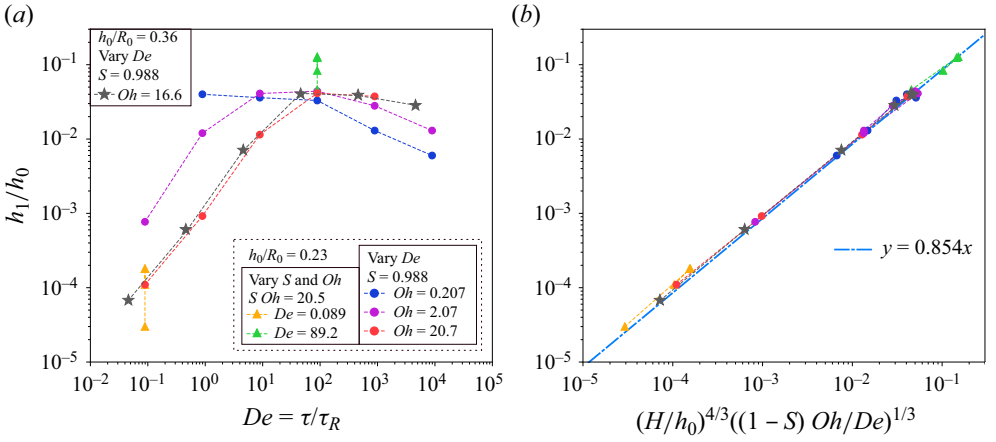

Figure 12. Numerical (non-dimensional) transition radius h_1/h_0 against (*a*) the Deborah number $De = \tau/\tau_R$, and (*b*) $(H/h_0)^{4/3}((1-S)\,Oh/De)^{1/3}$. The dash-dotted line in (*b*) is the line of equation $y = 0.854x$. The legend and range of parameters (Oh, De, S and h_0/R_0) are the same as in figure 11.

keeping $S\,Oh = \eta_s/\sqrt{\rho\gamma h_0}$ constant and equal to 9.88. In each case, S is varied between 0.1 and 0.988, where the total (constant shear) viscosity $\eta_0 = \eta_s + \eta_p$ is respectively dominated by the polymer and by the solvent contribution. All these additional data points in figure 11(*a*) rescale on the same curve identified in figure 11(*b*). This is because all these cases correspond to $Oh \gg 1$, where $\tau_{visc} = \eta_0 h_0/\gamma$ is the relevant time scale of the thinning dynamics in the Newtonian regime (and not $\eta_s h_0/\gamma$, for example), regardless of the value of S.

Additionally, a set of simulations was performed for a larger (non-dimensional) sample volume corresponding to $h_0/R_0 = 0.36$, varying De for fixed $Oh = 16.6$ and $S = 0.988$. These additional data points in figure 11(*a*) also rescale on the same curve identified in figure 11(*b*). This is because h_0 is the relevant length scale of the problem and sets τ_N (see (4.15)), in agreement with our experimental results, which show that h_1 increases when increasing the sample volume for a given plate diameter due to the increase in h_0 (see figure 4*b*).

We can finally test the prediction of (4.8) for the transition radius h_1 between the Newtonian and elastic regimes, which in non-dimensional terms reads

$$\frac{h_1}{h_0} = \left(\frac{H}{h_0}\right)^{4/3}\left[\frac{(1-S)\,Oh}{p\,De}\right]^{1/3}. \tag{4.16}$$

Figure 12(*a*) shows that h_1/h_0, which is estimated from the numerical h/h_0 curves for the same sets of parameters as in figure 11, does not monotonically increase or decrease with De. This is because at low De (more specifically at low $De_N = \tau/\tau_N$; see figure 11), $H/h_0 \propto De$ for $Oh \gg 1$ according to (4.12), implying that $h_1/h_0 \propto De$ according to (4.16), while at high De_N, $H/h_0 = 1$, implying that $h_1/h_0 \propto De^{-1/3}$ according to (4.16). We find that all values of h_1/h_0 indeed rescale on a single master curve when potted against $(H/h_0)^{4/3}((1-S)\,Oh/De)^{1/3}$ in figure 12(*b*), where we find that the value of p in (4.16) should be $p \approx 1.6$. Note that the value of p depends on the exact definition of h_1, since the transition between the Newtonian and elastic regimes is not necessarily sharp.

The validation of (4.16) proves that while (1.2) is valid for a fast plate separation protocol, relaxation of polymer chains must be taken into account to allow for values of $H < h_0$ for a slow plate separation protocol. It also proves that when we are interested in the minimum bridge/filament radius and maximum polymer extension at that point, the full two-dimensional problem can be reduced to a simple force balance equation such as (4.1) (which strictly applies only to a cylindrical thread) without losing predictive power, since (4.16) (or equivalently, (4.8)) is based on (4.1).

5. FENE-P prediction for h_1

We now consider how finite extensibility effects, described by the FENE-P model, can affect the transition radius $h_1 = h(t_1)$ at the onset of the elastic regime. We first derive a theoretical model validated by numerical simulations in § 5.1, before using it in § 5.2 to explain some of the discrepancies discussed in § 4.2 between the Oldroyd-B theory and experiments.

5.1. *Simulations and theory*

Figure 13(*a*) shows how, for fixed Oh, De, S and h_0/R_0, decreasing L^2 leads to an increase in h_1. This can be seen as counterintuitive since a decrease in L^2 implies that chains are shorter and therefore less elastic, which should imply a delayed transition to the elastic regime (smaller h_1). As we discuss in § 6, this apparent contradiction is resolved by considering that shorter chains have shorter relaxation times, leading to smaller values of H and therefore of h_1, which is not taken into account in the simulations of figure 13(*a*), where the Deborah number is kept constant.

Note that in figure 13(*a*), the thinning rate $|\dot{h}/h|$ in the elastic regime ($t > t_1$) is larger than $1/3\tau$ for the lowest L^2 values, while for the largest L^2 values, the elastic regime initially follows (1.1). This is because polymer chains are already close to being fully extended at the onset of the elastic regime for the lowest L^2 values, as discussed in our previous paper (Gaillard *et al.* 2024), where we explored the possibility of invoking this effect to explain variations of the apparent relaxation time τ_e (see e.g. figures 3*c*,*e*).

The reason why h_1 increases as L^2 decreases for a fixed De is because the elastic stress $\sigma_{p,zz} \approx GfA_{zz}$ (assuming $A_{zz} \gg 1$ at the transition; see (2.7*a*,*b*)) increases faster during the Newtonian regime ($t < t_1$) as L^2 decreases. This is because $f \approx 1/(1 - A_{zz}/L^2)$ (assuming $A_{zz} \gg 1 > A_{rr}$) diverges as A_{zz} approaches L^2 to model the stiffening of polymer chains as they approach full extension. Formally, assuming that the transition occurs when the elastic stress reaches a fraction p of the capillary pressure, i.e. when $\sigma_{p,zz} = p\gamma/h$ (where the $(2X - 1)$ prefactor is integrated into p; see § 4.1), we get

$$p\,\frac{\gamma}{h_1} = G\,\frac{A_1}{1 - A_1/L^2}, \tag{5.1}$$

where $h_1 = h(t_1)$ and $A_1 = A_{zz}(t_1)$ are the values at the transition. We assume that the bridge radius H marking the onset of the coil–stretch transition is unaffected by finite extensibility effects since A_{zz} is still close to 1 at the onset of this coil-stretch transition, i.e. $f \approx 1$. Assuming that relaxation becomes negligible between the onset of the coil–stretch transition and the onset of the elastic regime, i.e. for $h_1 < h < H$, we use $A_{zz} = (H/h)^4$ (see (4.6)), from which we get $A_1 = (H/h_1)^4$. Injecting this scaling into (5.1) leads to a

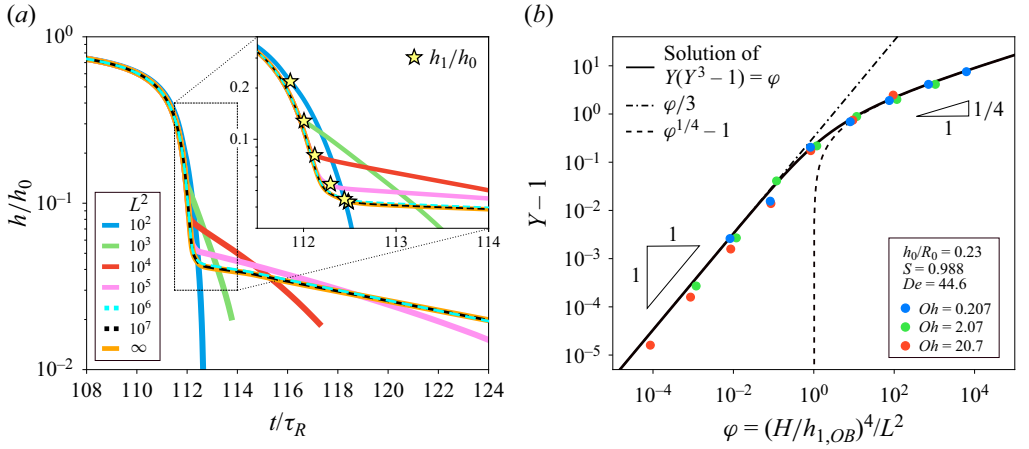

Figure 13. (*a*) Numerical time evolution of h/h_0 using the FENE-P model with L^2 ranging between 10^2 and 10^7, as well as $L^2 = +\infty$ (Oldroyd-B limit), for fixed $Oh = 2.07$, $De = 44.6$, $S = 0.988$ and $h_0/R_0 = 0.23$. The inset is a zoomed version for a better visualisation of the transition to the elastic regime at $h = h_1$. Simulations start at $t = 0$ used as the time reference. (*b*) Values of $Y - 1$ against φ (see (5.2*a–c*)) (where $Y = h_1/h_{1,OB}$, for $h_{1,OB}$ the Oldroyd-B limit of h_1) for L^2 ranging between 10^2 and 10^8, with $Oh = 0.207$, 2.07 and 20.7, and fixed values $De = 44.6$, $S = 0.988$ and $h_0/R_0 = 0.23$. Values are compared with the analytical solution of (5.2*a–c*) and with the limit scalings of (5.4).

polynomial equation for h_1 in the form

$$h_1 = h_{1,OB} \times Y(\varphi), \quad Y(Y^3 - 1) = \varphi, \quad \varphi = \frac{A_{1,OB}}{L^2}, \tag{5.2a–c}$$

where

$$h_{1,OB} = \left(\frac{GH^4}{p\gamma}\right)^{1/3} \quad \text{and} \quad A_{1,OB} = \left(\frac{H}{h_{1,OB}}\right)^4 \tag{5.3a,b}$$

are the values of h_1 and A_1 predicted in the Oldroyd-B limit $L^2 = +\infty$ ($\varphi = 0$); see (4.8) for $h_{1,OB}$. The two limit scalings of (5.2*a–c*) corresponding to weak ($\varphi \ll 1$) and strong ($\varphi \gg 1$) finite extensibility effects are

$$Y = \begin{cases} 1 + \varphi/3, & \text{for } \varphi \ll 1, \\ \varphi^{1/4}, & \text{for } \varphi \gg 1. \end{cases} \tag{5.4}$$

In the weak limit ($\varphi \ll 1$), polymer chains are still far from full extension at the onset of the elastic regime, while in the strong limit ($\varphi \gg 1$), the transition occurs significantly sooner than the Oldroyd-B prediction due to the fact that polymer chains have almost already reached full extension at the transition. Indeed, in the strong limit, the transition occurs when $A_{zz} = (H/h)^4$ becomes of the order of L^2, leading to

$$h_1 \sim \frac{H}{L^{1/2}}, \tag{5.5}$$

which is equivalent to (5.4) for $\varphi \gg 1$.

Values of Y estimated from numerical simulations using the FENE-P model are plotted against φ in figure 13(b) for three different Ohnesorge numbers, varying L^2 between 10^2 and 10^8 in each case, while keeping De, S and h_0/R_0 constant, using an extra Oldroyd-B simulation as a reference to get $h_{1,OB}$. We find that all data points collapse on a single curve corresponding to the solution of (5.2a–c). In particular, no prefactor is required in the $\varphi \gg 1$ limit. Note that we choose to plot $Y-1$ instead of Y in order to better visualise the $\varphi \ll 1$ regime. Note that the values of H/h_0, estimated for each simulation as in figure 10, are found not to depend on L^2, and take values between 1 and 0.36 for the data of figure 13(b). Equations (5.2a–c) therefore generalise (1.2) to cases where both finite extensibility effects and polymer relaxation effects are not negligible. In § 5.2, we apply this updated theory to rationalise some of the discrepancies discussed in § 4.2 between the Oldroyd-B theory and experiments.

5.2. *Experiments*

Experimentally, cases where both polymer relaxation and finite extensibility effects are expected to play a role correspond to low polymer concentrations c. Indeed, as c decreases, the transition to the elastic regime is delayed (i.e. h_1 decreases; see figures 5b and 6b) and polymer chains are therefore expected to be increasingly stretched at the onset of the elastic regime, assuming that their relaxation time becomes equal to the Zimm relaxation time τ_Z, which is independent of polymer concentration c (see (3.3)). Polymer chains should therefore ultimately approach full extension (at the onset of the elastic regime) below a critical concentration c_{low} introduced by Campo-Deano & Clasen (2010). For $c < c_{low}$, the elasto-capillary balance leading to the exponential decay of (1.1) is therefore no longer valid since $A_1 \sim L^2$, leading to filament thinning rates $|\dot{h}/h| > 1/3\tau$, as shown numerically in figure 13(a) and discussed in our previous paper (Gaillard *et al.* 2024). This would explain why fitting the elastic regime ($t > t_1$) with a exponential leads to apparent relaxation times τ_e that are smaller than τ_Z, as reported in figure 6(a) for aqueous PEO-4M solutions of concentrations $c \leq 10$ ppm. This would also explain why, as discussed in § 4.2 (see triangle symbols in figure 9b), transition radii h_1 measured for low polymer concentrations cannot be captured by the Oldroyd-B prediction even when replacing values of $\tau_e < \tau_Z$ by τ_Z.

This idea is tested in figure 14, where experimentally measured values of h_1 ($h_{1,exp}$) are plotted against the FENE-P theoretical prediction $h_{1,th} = h_{1,OB} \times Y(\varphi)$ (see (5.2a–c) and (5.3a,b)) for all polymer solutions and initial bridge radii. We choose $L^2 = \infty$ ($Y = 1$) and $\tau = \tau_e$ as model parameters for data points corresponding to the PEO_{aq} (1 and 2, 500 ppm PEO-4M solution in water), PEO_{visc} (1 and 2, 25 ppm PEO-4M solution in a more viscous solvent) and HPAM solutions, since we already know from figure 9(b) that these h_1 values are consistent with the Oldroyd-B prediction of (4.8) (we choose $p = 0.27$ to match the prefactor found in figure 9b). The experimentally measured values of h_1 corresponding to aqueous PEO-4M solutions of various concentrations in figure 14 (orange triangle symbols) are higher than the Oldroyd-B prediction at low concentrations, as we saw in figure 9(b), where replacing values of $\tau_e < \tau_Z$ by τ_Z was found to be insufficient to explain the discrepancy. The blue triangle symbols in figure 14 show that this discrepancy can be rationalised using the FENE-P model, where we chose a value $L^2 = 1 \times 10^4$ that is sufficiently small to allow for values of Y sufficiently larger than 1 (i.e. polymer chains close to being fully extended at the onset of the elastic regime) to 'fill the remaining gap', while using $\tau = \max(\tau_e, \tau_Z)$ at the model relaxation time.

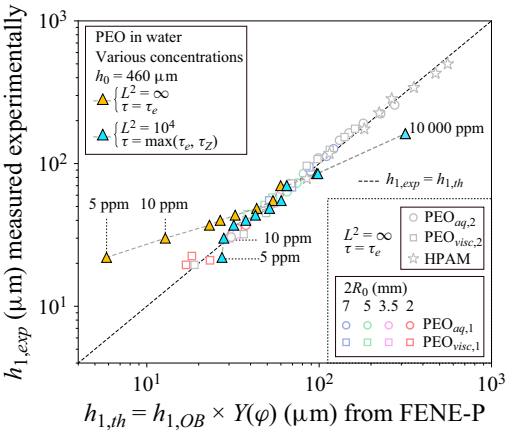

Figure 14. Experimentally measured h_1 values ($h_{1,exp}$) against the FENE-P theoretical prediction $h_{1,th} = h_{1,OB} \times Y(\varphi)$ (see (5.2*a–c*) and (5.3*a*,*b*)) for various polymer solutions and initial bridge radii. Values of the FENE-P model parameters τ and L^2 are indicated in the legends (η_p values are the ones from shear rheology). The discrepancy between experiments and the Oldroyd-B prediction for h_1 at low polymer concentration can be rationalised by finite extensibility effects; see main text.

This value $L^2 = 1 \times 10^4$ has the same order of magnitude as the value expected from the microscopic formula (Clasen *et al.* 2006*b*)

$$L^2 = 3\left[\frac{j \sin^2(\theta/2)\, M_w}{C_\infty\, M_u}\right]^{2(1-\nu)}, \tag{5.6}$$

which gives L^2 between 1.6×10^4 and 1.3×10^5 for PEO of molecular weight $M_w = 4 \times 10^6\,\mathrm{g\,mol^{-1}}$, for solvent quality exponents ν between 3/5 (good solvent) and 1/2 (theta solvent), where M_u is the monomer molecular weight, $\theta = 109^\circ$ is the C-C bond angle, $j = 3$ is the number of bonds of a monomer, and $C_\infty = 4.8$ is the characteristic ratio (Brandrup & Immergut 1999). Assuming that ν is between 1/2 and 3/5, the discrepancy can be explained by a value M_w less than $4 \times 10^6\,\mathrm{g\,mol^{-1}}$ stemming from polymer degradation during mixing when preparing the stock solution. Note that choosing $L^2 = 1 \times 10^4$ leads to values of Y close to 1 (up to 1.18) for the PEO_{aq} (1 and 2), PEO_{visc} (1 and 2) and HPAM solutions, consistent with the agreement between experiments and the Oldroyd-B theory for these solutions in figure 14, as shown by the small difference between the $L^2 = \infty$ (orange) and $L^2 = 1 \times 10^4$ (blue) triangle symbols for $c = 500$ ppm, which corresponds to the $PEO_{aq,1}$ solution.

6. Conclusions and discussions

We have shown experimentally that the classical formula (1.2) for the bridge/filament radius h_1 marking the onset of the elastic regime does not hold for slow filament thinning techniques such as CaBER with a slow plate separation protocol. This is because, unlike what is assumed to derive (1.2), polymer chains do not necessarily start stretching (beyond their equilibrium coiled configuration) at the threshold of the Rayleigh–Plateau instability (with minimum bridge radius h_0), but do so only when the bridge thinning rate becomes comparable to the inverse of their relaxation time. This leads to the generalised formula (4.8) with a scaling $h_1 \propto H^{4/3}$, where H is the bridge radius marking the onset of the coil–stretch transition in the Newtonian regime. This formula reconciles the large

relaxation time limit $H = h_0$, where (1.2) is recovered, with the low relaxation time limit anticipated by Campo-Deano & Clasen (2010), where polymer chains start stretching only when the bridge thinning dynamics has become self-similar, in which case H (and therefore h_1) becomes independent of h_0 (see (4.11)–(4.14)). Our generalised formula has been validated experimentally in § 4.2 for different polymer solutions (PEO, HPAM) and solvent viscosities (covering both inertio- and visco-capillary thinning dynamics in the Newtonian regime), and for a wide range of plate diameters and sample volumes. This generalised formula is in principle valid for any pinch-off experiment, e.g. dripping or DoS experiments, provided that polymer chains are relaxed at the onset of capillary thinning (no pre-stress). This universality comes from the fact that H is an intrinsic length scale of the problem that transcends the particularities of the protocol used to perform a pinch-off experiment, unlike the last stable bridge radius h_0, which is defined only for our particular protocol. Understanding how H scales with the parameters of the problem is therefore crucial in order to predict h_1, and the discussion of § 4.3 on the dependence of H/h_0 on the Deborah and Ohnesorge numbers is applicable only to our specific protocol.

The Oldroyd-B formula (4.8) was extended to finitely extensible polymer chains using a FENE-P description. This updated theory, accounting for both polymer relaxation and finite extensibility, was found to be able to rationalise the discrepancies observed for the lowest PEO concentrations between the Oldroyd-B theory and experimental values of h_1. This is consistent with the fact that apparent relaxation times τ_e less than the Zimm relaxation time τ_Z were measured at these low concentrations, an anomaly also reported by Campo-Deano & Clasen (2010) that stems from polymer chains being close to full extension at the onset of the elastic regime, a case where (1.1) is no longer valid and thinning rates $|\dot{h}/h| > 1/3\tau$ are observed, as we discuss in our previous paper (Gaillard *et al.* 2023). The polymer concentration c_{low} below which chains are close to full extension at the onset of the elastic regime ($A_1 \sim L^2$) corresponds to $\varphi = 1$ (see (5.2*a–c*)), which gives an elastic modulus $G_{low} = p\gamma/HL^{3/2}$ that can be converted into a concentration using $G = cN_Ak_BT/M_w$ (Campo-Deano & Clasen 2010). This expression generalises the expression of Campo-Deano & Clasen (2010) (who considered the limiting case of low relaxation times and low solvent viscosities) to any Deborah and Ohnesorge numbers since H is a function of these numbers.

The Oldroyd-B formula (4.8) solves an apparent paradox of (1.2) that predicts that the transition to the elastic regime occurs sooner as polymer chains get shorter for a fixed (mass) concentration. Indeed, (1.2) predicts $h_1 \propto G^{1/3}$, where the elastic modulus scales with molecular weight as $G \propto M_w^{-1}$ (Clasen *et al.* 2006*b*), yielding $h_1 \propto M_w^{-1/3}$, which increases as M_w decreases. This is counterintuitive since shorter chains should imply lower elasticity and therefore a delayed transition, h_1 approaching 0 as polymer chains approach monomer size. This apparent paradox is solved by realising that shorter chains have a shorter (Zimm) relaxation time since $\tau_Z \propto M_w^{3\nu}$ (Clasen *et al.* 2006*b*), where ν is the solvent quality exponent, implying that H (see (4.8)) should start decreasing as M_w decreases for sufficiently low Deborah numbers (see figure 11). In the low-relaxation-time (equivalently low-M_w) limit where polymer chains start stretching only when the bridge thinning dynamics has become self-similar, we get $h_1 \propto M_w^{(8\nu-1)/3}$ for $Oh \ll 1$, and $h_1 \propto M_w^{(12\nu-1)/3}$ for $Oh \gg 1$, according to (4.13) and (4.14), both exponents being positive for any ν between 1/2 (theta solvent) and 3/5 (good solvent), which solves the apparent paradox. This remains true even in the limit where polymer chains are almost fully extended at the onset of the elastic regime since (5.5) predicts $h_1 \propto M_w^{(5\nu-1)/2}$ for $Oh \ll 1$,

and $h_1 \propto M_w^{(7\nu-1)/2}$ for $Oh \gg 1$, according to (4.11) and (4.12) for H, using $L \propto M_w^{1-\nu}$ (see (5.6)).

Our work suggests that a FENE-P description is sufficient to predict the transition radius h_1 to the elastic regime provided that the apparent relaxation time τ_e, measured from an exponential fit of $h(t)$ in the elastic regime, is chosen as 'the' relaxation time of the polymer solution or, more precisely, $\max(\tau_e, \tau_Z)$ (see § 5.2). However, the surprising increase of τ_e with h_0 (see figure 4*a*) cannot be rationalised using a FENE-P description, as detailed in our previous paper (Gaillard *et al.* 2024), where we chose the high-h_0 limit of τ_e, named τ_m, as 'the' relaxation time. The results of this study allow us to further comment on whether it is τ_e or τ_m that should be considered as the 'true' relaxation time, if any. Indeed, we saw in § 4.2 that using τ_m as 'the' relaxation time instead of τ_e works only for the PEO_{visc} solution, i.e. the most dilute one in the most viscous solvent. This would suggest that it is τ_e (and not τ_m) that is the 'true' relaxation time since it can be used to predict h_1 for any solution. However, if τ_e really measures the 'true' relaxation, then it implies that some rheological property of a polymer solution somehow 'changes' when being tested with a different system size (plate diameter and sample volume) via a mechanism that we could not identify and which is unlikely to be evaporation or polymer degradation (Gaillard *et al.* 2024). Another possibility is that the solution in fact does not change, meaning that the system-size dependence of τ_e is not an artefact, in which case it would be only by coincidence that we could successfully capture experimental values of h_1 using τ_e. This would imply that the Oldroyd-B and FENE-P models miss some important features of polymer dynamics in extensional flows, strengthening the already established need for better constitutive equations. Future works will determine if more sophisticated models such as conformation-dependent drag models, accounting for the action of both chain stretching and intermolecular hydrodynamic interactions on the friction coefficient (Prabhakar *et al.* 2016, 2017), are able to rationalise our experimental results on the system-size dependence of both τ_e and h_1.

Funding. M.A.H. acknowledges funding from the Spanish Ministry of Economy, Industry and Competitiveness under grant PID2022-140951O.

Declaration of interests. The authors report no conflict of interest.

Author ORCIDs.
A. Gaillard https://orcid.org/0000-0003-1775-2682;
M.A. Herrada https://orcid.org/0000-0003-0388-8001;
A. Deblais https://orcid.org/0000-0002-3574-2480;
J. Eggers https://orcid.org/0000-0002-0011-5575;
D. Bonn https://orcid.org/0000-0001-8925-1997.

Appendix. Filament length L_f

The filament length L_f, introduced in the right-hand inset of figure 2(*a*), is plotted in figure 15 against the initial bridge radius h_0 for all polymer solutions, plate diameters $2R_0$, and (non-dimensional) sample volumes V^* considered in this study. All data points collapse on a single curve, indicating that L_f does not depend on rheological properties. This is particularly true for data points corresponding to different PEO concentrations in water where, since h_0 is kept constant by keeping the same plate diameter and sample volume, the filament length also remains constant. This is easily understood by considering that the filament length actually corresponds to the distance between the top and bottom end drops after pinch-off (i.e. after rupture of the filament), which should be the same

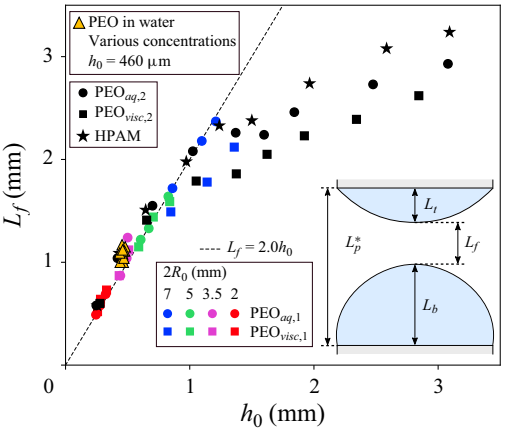

Figure 15. Filament length L_f against the initial bridge radius h_0 for all polymer solutions, plate diameters and sample volumes. The inset shows a sketch of the top and bottom end drops after pinch-off.

regardless of the bulk mechanical properties of the liquid (as long as the plates are separated slowly). This distance can be expressed as $L_f = L_p^* - L_t - L_b$, where L_p^* is the final plate separation distance, L_t is the distance between the top plate and the bottom of the top end drop, and L_b ($\geq L_t$ due to gravity) is the distance between the bottom plate and the top of the bottom end drop; see the inset of figure 15. Note that our protocol is such that L_p^* is the critical plate separation distance at which the bridge becomes unstable to the Rayleigh–Plateau instability. All these quantities should indeed be functions only of the Bond number $Bo = \rho g R_0^2/\gamma$, of V^*, and of the contact angle of the liquid with the plates. We find that $L_f \approx 2.1h_0$ for plates of diameters typically $2R_0 \leq 7$ mm, while lower L_f values are observed for larger plates. This might be caused by the dewetting of the top plate which, as discussed in § 2.3, could not be avoided for such large plates in spite of the plasma treatment, hence resulting in a smaller 'effective' top plate, which might result in values of L_p^* lower than expected. The scatter in data points for these large plates might hence be due to differences in the amount of dewetting.

References

Amarouchene, Y., Bonn, D., Meunier, J. & Kellay, H. 2001 Inhibition of the finite-time singularity during droplet fission of a polymeric fluid. *Phys. Rev. Lett.* **86**, 3558–3561.

Anna, S.L. & McKinley, G.H. 2001 Elasto-capillary thinning and breakup of model elastic liquids. *J. Rheol.* **45** (1), 115–138.

Bazilevsky, A.V., Entov, V.M., Lerner, M.M. & Rozhkov, A.N. 1997 Failure of polymer solution filaments. *Polym. Sci.* A **39** (3), 316–324.

Bazilevsky, A.V., Entov, V.M. & Rozhkov, A.N. 2001 Breakup of an Oldroyd liquid bridge as a method for testing the rheological properties of polymer solutions. *Polym. Sci. AC/C Vysokomol. Soedin.* **43** (7), 716–726.

Boyko, E. & Stone, H.A. 2024 Perspective on the description of viscoelastic flows via continuum elastic dumbbell models. *J. Engng Maths* **147** (1), 5.

Brandrup, J. & Immergut, E.H. 1999 *Polymer Handbook*. John Wiley & Sons.

Campo-Deano, L. & Clasen, C. 2010 The slow retraction method (SRM) for the determination of ultra-short relaxation times in capillary breakup extensional rheometry experiments. *J. Non-Newtonian Fluid Mech.* **165** (23–24), 1688–1699.

Casanellas, L., Alves, M.A., Poole, R.J., Lerouge, S. & Lindner, A. 2016 The stabilizing effect of shear thinning on the onset of purely elastic instabilities in serpentine microflows. *Soft Matt.* **12** (29), 6167–6175.

CHRISTANTI, Y. & WALKER, L.M. 2002 Effect of fluid relaxation time of dilute polymer solutions on jet breakup due to a forced disturbance. *J. Rheol.* **46** (3), 733–748.

CLASEN, C., BICO, J., ENTOV, V.M. & MCKINLEY, G.H. 2009 Gobbling drops: the jetting–dripping transition in flows of polymer solutions. *J. Fluid Mech.* **636**, 5–40.

CLASEN, C., EGGERS, J., FONTELOS, M.A., LI, J.I.E. & MCKINLEY, G.H. 2006*a* The beads-on-string structure of viscoelastic threads. *J. Fluid Mech.* **556**, 283–308.

CLASEN, C., PLOG, J.P., KULICKE, W.-M., OWENS, M., MACOSKO, C., SCRIVEN, L.E., VERANI, M. & MCKINLEY, G.H. 2006*b* How dilute are dilute solutions in extensional flows? *J. Rheol.* **50** (6), 849–881.

DEBLAIS, A., HERRADA, M.A., HAUNER, I., VELIKOV, K.P., VAN ROON, T., KELLAY, H., EGGERS, J. & BONN, D. 2018 Viscous effects on inertial drop formation. *Phys. Rev. Lett.* **121** (25), 254501.

DINIC, J., JIMENEZ, L.N. & SHARMA, V. 2017 Pinch-off dynamics and dripping-onto-substrate (DoS) rheometry of complex fluids. *Lab on a Chip* **17** (3), 460–473.

DINIC, J. & SHARMA, V. 2019 Macromolecular relaxation, strain, and extensibility determine elastocapillary thinning and extensional viscosity of polymer solutions. *Proc. Natl Acad. Sci. USA* **116** (18), 8766–8774.

EGGERS, J. 1993 Universal pinching of 3D axisymmetric free-surface flow. *Phys. Rev. Lett.* **71** (21), 3458.

EGGERS, J. 1997 Nonlinear dynamics and breakup of free-surface flows. *Rev. Mod. Phys.* **69** (3), 865.

EGGERS, J. 2014 Instability of a polymeric thread. *Phys. Fluids* **26** (3), 033106.

EGGERS, J., HERRADA, M.A. & SNOEIJER, J.H. 2020 Self-similar breakup of polymeric threads as described by the Oldroyd-B model. *J. Fluid Mech.* **887**, A19.

ENTOV, V.M. & HINCH, E.J. 1997 Effect of a spectrum of relaxation times on the capillary thinning of a filament of elastic liquid. *J. Non-Newtonian Fluid Mech.* **72** (1), 31–53.

GAILLARD, A., HERRADA, M.A., DEBLAIS, A., EGGERS, J. & BONN, D. 2024 Beware of CaBER: filament thinning rheometry does not always give 'the' relaxation time of polymer solutions. *Phys. Rev. Fluids* **9** (7), 073302.

GAILLARD, A., SIJS, R. & BONN, D. 2022 What determines the drop size in sprays of polymer solutions? *J. Non-Newtonian Fluid Mech.* **305**, 104813.

GIDRETA, B.T. & KIM, H. 2023 Effects of physical property changes of expelled respiratory liquid on atomization morphology. *J. Fluid Mech.* **960**, A10.

GILÁNYI, T., VARGA, I., GILÁNYI, M. & MÉSZÁROS, R. 2006 Adsorption of poly (ethylene oxide) at the air/water interface: a dynamic and static surface tension study. *J. Colloid Interface Sci.* **301** (2), 428–435.

GRAESSLEY, W.W. 1980 Polymer chain dimensions and the dependence of viscoelastic properties on concentration, molecular weight and solvent power. *Polymer* **21** (3), 258–262.

HERRADA, M.A. & MONTANERO, J.M. 2016 A numerical method to study the dynamics of capillary fluid systems. *J. Comput. Phys.* **306**, 137–147.

INGREMEAU, F. & KELLAY, H. 2013 Stretching polymers in droplet-pinch-off experiments. *Phys. Rev.* X **3** (4), 041002.

KESHAVARZ, B., HOUZE, E.C., MOORE, J.R., KOERNER, M.R. & MCKINLEY, G.H. 2016 Ligament mediated fragmentation of viscoelastic liquids. *Phys. Rev. Lett.* **117** (15), 154502.

KESHAVARZ, B., SHARMA, V., HOUZE, E.C., KOERNER, M.R., MOORE, J.R., COTTS, P.M., THRELFALL-HOLMES, P. & MCKINLEY, G.H. 2015 Studying the effects of elongational properties on atomization of weakly viscoelastic solutions using Rayleigh Ohnesorge Jetting Extensional Rheometry (ROJER). *J. Non-Newtonian Fluid Mech.* **222**, 171–189.

LI, Y. & SPRITTLES, J.E. 2016 Capillary breakup of a liquid bridge: identifying regimes and transitions. *J. Fluid Mech.* **797**, 29–59.

MACOSKO, C.W. 1994 *Rheology: Principles, Measurements, and Applications*. Wiley-VCH.

MCKINLEY, G.H. & TRIPATHI, A. 2000 How to extract the Newtonian viscosity from capillary breakup measurements in a filament rheometer. *J. Rheol.* **44** (3), 653–670.

MILLER, E., CLASEN, C. & ROTHSTEIN, J.P. 2009 The effect of step-stretch parameters on capillary breakup extensional rheology (CaBER) measurements. *Rheol. Acta* **48**, 625–639.

MONTANERO, J.M. & PONCE-TORRES, A. 2020 Review on the dynamics of isothermal liquid bridges. *Appl. Mech. Rev.* **72** (1), 010803.

PAPAGEORGIOU, D.T. 1995 On the breakup of viscous liquid threads. *Phys. Fluids* **7** (7), 1529–1544.

PHAN-THIEN, N., MANERO, O. & LEAL, L.G. 1984 A study of conformation-dependent friction in a dumbbell model for dilute solutions. *Rheol. Acta* **23**, 151–162.

PINGULKAR, H., PEIXINHO, J. & CRUMEYROLLE, O. 2021 Liquid transfer for viscoelastic solutions. *Langmuir* **37** (34), 10348–10353.

PRABHAKAR, R., GADKARI, S., GOPESH, T. & SHAW, M.J. 2016 Influence of stretching induced self-concentration and self-dilution on coil–stretch hysteresis and capillary thinning of unentangled polymer solutions. *J. Rheol.* **60** (3), 345–366.

PRABHAKAR, R., SASMAL, C., NGUYEN, D.A., SRIDHAR, T. & PRAKASH, J.R. 2017 Effect of stretching-induced changes in hydrodynamic screening on coil–stretch hysteresis of unentangled polymer solutions. *Phys. Rev. Fluids* **2** (1), 011301.

RAJESH, S., THIÉVENAZ, V. & SAURET, A. 2022 Transition to the viscoelastic regime in the thinning of polymer solutions. *Soft Matt.* **18** (16), 3147–3156.

RODD, L.E., SCOTT, T.P., COOPER-WHITE, J.J. & MCKINLEY, G.H. 2005 Capillary break-up rheometry of low-viscosity elastic fluids. *Appl. Rheol.* **15** (1), 12–27.

SATTLER, R., GIER, S., EGGERS, J. & WAGNER, C. 2012 The final stages of capillary break-up of polymer solutions. *Phys. Fluids* **24** (2), 023101.

SATTLER, R., WAGNER, C. & EGGERS, J. 2008 Blistering pattern and formation of nanofibers in capillary thinning of polymer solutions. *Phys. Rev. Lett.* **100** (16), 164502.

SCHARFMAN, B.E., TECHET, A.H., BUSH, J.W.M. & BOUROUIBA, L. 2016 Visualization of sneeze ejecta: steps of fluid fragmentation leading to respiratory droplets. *Exp. Fluids* **57** (2), 1–9.

SEMAKOV, A.V., KULICHIKHIN, V.G., TERESHIN, A.K., ANTONOV, S.V. & MALKIN, A.Y. 2015 On the nature of phase separation of polymer solutions at high extension rates. *J. Polym. Sci.* B*: Polym. Phys.* **53** (8), 559–565.

SEN, U., DATT, C., SEGERS, T., WIJSHOFF, H., SNOEIJER, J.H., VERSLUIS, M. & LOHSE, D. 2021 The retraction of jetted slender viscoelastic liquid filaments. *J. Fluid Mech.* **929**, A25.

SLOBOZHANIN, L.A. & PERALES, J.M. 1993 Stability of liquid bridges between equal disks in an axial gravity field. *Phys. Fluids* A*: Fluid Dyn.* **5** (6), 1305–1314.

SMITH, D.E., BABCOCK, H.P. & CHU, S. 1999 Single-polymer dynamics in steady shear flow. *Science* **283** (5408), 1724–1727.

SNOEIJER, J.H., PANDEY, A., HERRADA, M.A. & EGGERS, J. 2020 The relationship between viscoelasticity and elasticity. *Proc. R. Soc. Lond.* A **476**, 20200419.

STELTER, M., BRENN, G., YARIN, A.L., SINGH, R.P. & DURST, F. 2000 Validation and application of a novel elongational device for polymer solutions. *J. Rheol.* **44** (3), 595–616.

STELTER, M., BRENN, G., YARIN, A.L., SINGH, R.P. & DURST, F. 2002 Investigation of the elongational behavior of polymer solutions by means of an elongational rheometer. *J. Rheol.* **46** (2), 507–527.

TIRTAATMADJA, V., MCKINLEY, G.H. & COOPER-WHITE, J.J. 2006 Drop formation and breakup of low viscosity elastic fluids: effects of molecular weight and concentration. *Phys. Fluids* **18** (4), 043101.

VERBEKE, K., FORMENTI, S., VANGOSA, F.B., MITRIAS, C., REDDY, N.K., ANDERSON, P.D. & CLASEN, C. 2020 Liquid bridge length scale based nondimensional groups for mapping transitions between regimes in capillary break-up experiments. *Phys. Rev. Fluids* **5** (5), 051901.

WAGNER, C., AMAROUCHENE, Y., BONN, D. & EGGERS, J. 2005 Droplet detachment and satellite bead formation in viscoelastic fluids. *Phys. Rev. Lett.* **95** (16), 164504.

WAGNER, C., BOUROUIBA, L. & MCKINLEY, G.H. 2015 An analytic solution for capillary thinning and breakup of FENE-P fluids. *J. Non-Newtonian Fluid Mech.* **218**, 53–61.

ZELL, A., GIER, S., RAFAI, S. & WAGNER, C. 2010 Is there a relation between the relaxation time measured in CaBER experiments and the first normal stress coefficient? *J. Non-Newtonian Fluid Mech.* **165** (19), 1265–1274.